

1 Overview of observations from the RADAGAST experiment in Niamey, Niger.

2 Part 2: Radiative fluxes and divergences

3  
4 A. Slingo, H. E. White, N. A. Bharmal and G. J. Robinson

5 Environmental Systems Science Centre, University of Reading, UK

6  
7 22 May 2008

8  
9 **Abstract**

10 Broadband shortwave and longwave radiative fluxes observed both at the surface and  
11 from space during the RADAGAST experiment in Niamey, Niger in 2006 are  
12 presented. The surface fluxes were measured by the Atmospheric Radiation  
13 Measurement (ARM) Program Mobile Facility (AMF) at Niamey airport, while the  
14 fluxes at the top of the atmosphere (TOA) are from the Geostationary Earth Radiation  
15 Budget (GERB) instrument on the Meteosat-8 satellite. The data are analyzed as daily  
16 averages, in order to minimise sampling differences between the surface and top of  
17 atmosphere instruments, while retaining the synoptic and seasonal changes that are  
18 the main focus of this study. A cloud mask is used to identify days with cloud from  
19 those with predominantly clear skies.

20 The influence of temperature, water vapor, aerosols and clouds is investigated.  
21 Aerosols are ubiquitous throughout the year and have a significant impact on both the  
22 shortwave and longwave fluxes. The large and systematic seasonal changes in  
23 temperature and column integrated water vapor (CWV) through the dry and wet  
24 seasons are found to exert strong influences on the longwave fluxes. These influences  
25 are often in opposition to each other, because the highest temperatures occur at the  
26 end of the dry season when the CWV is lowest, while in the wet season the lowest  
27 temperatures are associated with the highest values of CWV. Apart from aerosols, the  
28 shortwave fluxes are also affected by clouds and by the seasonal changes in CWV.

29 The fluxes are combined to provide estimates of the divergence of radiation across  
30 the atmosphere throughout 2006. The longwave divergence is remarkably constant

31 through the year, because of a compensation between the seasonal variations in the  
32 outgoing longwave radiation (OLR) and surface net longwave radiation. A simple  
33 model of the greenhouse effect is used to interpret this result in terms of the  
34 dependence of the normalized greenhouse effect at the TOA and of the effective  
35 emissivity of the atmosphere at the surface on the CWV. It is shown that, as the CWV  
36 increases, the atmosphere loses longwave energy to the surface with about the same  
37 increasing efficiency with which it traps the OLR, thus keeping the atmospheric  
38 longwave divergence roughly constant. The shortwave divergence is mainly  
39 determined by the CWV and aerosol loadings and the effect of clouds is much  
40 smaller than on the component fluxes.

41

## 42 **1. Introduction**

43 Radiative processes are of crucial importance in determining the basic characteristics of the  
44 climate system, its stability and its response to perturbations. Understanding the radiation budget  
45 and what controls it is central to climate science, because changes in the budget are driving  
46 climate change and are also involved in the associated feedbacks [Randall *et al.*, 2007]. In recent  
47 decades, satellite observations have provided an accurate description of the radiation budget at  
48 the top of the atmosphere (TOA) and its seasonal and interannual variability [Wong *et al.*, 2006;  
49 Loeb *et al.*, 2007]. In contrast, the radiation budget at the surface is less well observed, because  
50 almost all of the long-term observing sites are over land and their spatial distribution is very  
51 heterogeneous [Ohmura *et al.*, 1998]. Retrievals of the surface radiation budget over the whole  
52 globe are now available from satellite data, using additional datasets and modeling, which have  
53 been validated against the surface sites [Zhang *et al.*, 2004; Stackhouse *et al.*, 2004].  
54 Nevertheless, estimates of the divergence of radiation across the atmosphere, obtained by  
55 differencing the radiation budget at the surface from that at the TOA, show significant variations  
56 depending on the datasets employed. For example, estimates of the global and annual mean  
57 shortwave (solar) radiation absorbed by the atmosphere vary from 67 to 93  $\text{Wm}^{-2}$  [Kiehl and  
58 Trenberth, 1997; Ramana *et al.*, 2007]. Significant differences also exist between estimates of the  
59 longwave divergence across the atmosphere, even for clear-skies [Allan, 2006; and references  
60 therein].

61 One approach to making progress in characterizing the atmospheric divergence and in  
62 understanding what controls it is to combine radiative fluxes and other measurements from a  
63 single, well-instrumented surface site with satellite data. Unfortunately, until recently, all broad-  
64 band satellite radiometers have flown in low Earth orbits, so the availability of data over a given  
65 surface site has been limited in its temporal resolution and diurnal coverage. This situation  
66 improved dramatically with the launch of the first Geostationary Earth Radiation Budget (GERB)  
67 instrument on the Meteosat-8 European weather satellite in August 2002 [Harries *et al.*, 2005].  
68 GERB provides broad-band shortwave and longwave fluxes every 15 minutes at about 50km  
69 resolution within the Meteosat field of view. Building on this advance, a proposal was submitted  
70 to the U.S. Department of Energy's Atmospheric Radiation Measurement (ARM) Program to  
71 deploy their new ARM Mobile Facility (AMF) to Niamey, the capital of Niger in West Africa, to  
72 make coordinated measurements with GERB in collaboration with the African Monsoon  
73 Multidisciplinary Analysis (AMMA) experiment [Redelsperger *et al.*, 2006], the field phases of  
74 which were due to take place in 2006. This proposal was called RADAGAST (Radiative  
75 Atmospheric Divergence using ARM Mobile Facility, GERB data and AMMA STations).  
76 Further details on the background to the AMF and its deployment to Niger for the RADAGAST  
77 experiment are provided by Miller and Slingo [2007].

78 The African continent provides a unique environment within which to study the physical  
79 processes that control the radiation budget. North Africa is the most important source of wind-  
80 blown dust in the world [Prospero *et al.*, 2002] and the burning of vegetation in the dry seasons  
81 to clear the ground for crops can lead to high loadings of biomass aerosols. The extended drought  
82 that occurred in the Sahel in the 1970s and 1980s [Bell and Lamb, 2006] stimulated extensive  
83 research to discover the cause, which included the suggestion that radiative and biogeophysical  
84 feedbacks could be involved [Charney, 1975]. The climate of the Sahel is strongly influenced by  
85 the West African monsoon, which regulates the seasonal cycle of dry and wet seasons in response  
86 to the changing solar forcing. This important system was the focus of the AMMA observations in  
87 2006. In association with AMMA, several focused experiments studied various aspects of the  
88 monsoon. In particular, the DABEX experiment built on previous airborne campaigns to make *in*  
89 *situ* measurements of the radiative properties of wind-blown dust and of aerosols from biomass  
90 burning in the dry season [Haywood *et al.*, 2008].

91 An overview of the RADAGAST observations of the meteorology and thermodynamic variables

92 is provided in a companion paper [*Slingo et al.*, 2008; hereafter Part 1]. Here, the focus is on the  
93 radiative fluxes both at the top of the atmosphere (TOA) and at the surface, and on the first direct  
94 estimates of the divergence of radiation across the atmosphere. The surface fluxes were measured  
95 by the AMF at the main Niamey airport site (13° 29'N, 2° 10'E). The TOA fluxes were measured  
96 by the GERB broadband radiometer on Meteosat-8, stationed above 0° longitude.

97 In contrast to previous field studies that have invariably been of short duration, this paper  
98 presents the radiative fluxes and derived divergences for the whole of 2006, and investigates the  
99 influences of controlling factors such as temperature, water vapor, clouds and aerosols. These  
100 results are the first estimates of broadband radiative divergences using both surface and satellite  
101 observations that are available both at high temporal resolution and for such an extended period  
102 of time. The philosophy of the approach taken in the analysis is to avoid the use of detailed  
103 radiative transfer modeling, since this is the remit of some of the following papers in this special  
104 section. Rather, the emphasis is on presenting the timeseries of the various radiative quantities  
105 and to use scatter plots, simple models and to a limited degree the results from the other studies  
106 to identify the main factors that control the fluxes and divergences.

107 Many difficult sampling issues arise when bringing together measurements from the surface and  
108 from space to calculate atmospheric flux divergences above a single location [*Settle et al.*, 2008].  
109 We minimize these issues in this first study of the divergences from RADAGAST by using daily  
110 averaged data and by analyzing only the divergences across the atmosphere as a whole, as  
111 opposed to the vertical structure of the divergences within the atmosphere. As a result, the effects  
112 of residual sampling uncertainties and of errors in the calibration of the instruments are much  
113 smaller than the magnitude of the divergences themselves, so they have a much less damaging  
114 impact on the analysis than would be the case for data with higher time and space resolution.

115 In the following section, the data used and the processing are described. Section 3 presents  
116 timeseries of cloud and aerosol retrievals that are used later to investigate their influence on the  
117 fluxes and divergences. Timeseries of the radiative fluxes from the AMF at the surface and from  
118 GERB at the TOA are analyzed in Section 4. Scatter plots are used in Section 5 to investigate the  
119 relative roles of temperature, water vapor, clouds and aerosols on the fluxes. The derived  
120 divergences are presented in Section 6, both as timeseries and as scatter plots, which are used to  
121 explore the factors that control the divergences. The longwave fluxes and divergences are

122 analyzed further in Section 7 using a simple model of the greenhouse effect. Finally, Section 8  
123 summarizes and discusses the main results of this work.

## 124 **2. Data sources, processing and errors**

### 125 **2.1. Radiative fluxes**

126 Upwelling and downwelling longwave (thermal) and shortwave (solar) radiative fluxes measured  
127 at the surface were obtained from the radiometers at the main Niamey airport site. Details of the  
128 AMF instruments and of their characteristics are given by *Miller and Slingo* [2007]. The total  
129 downwelling shortwave radiation was calculated using the component sum method [*Michalsky et*  
130 *al.*, 1999], whereby the direct flux measured normal to the direction of the sun is multiplied by  
131 the cosine of the solar zenith angle and added to the measured diffuse flux. This provides a more  
132 accurate estimate of the total downwelling flux than a measurement of the sum of the direct and  
133 diffuse fluxes by a single radiometer.

134 Outgoing longwave radiation (OLR) and reflected shortwave radiation at the TOA were obtained  
135 from the GERB instrument on Meteosat-8 [*Harries et al.*, 2005]. Version 3 ARG data from  
136 GERB were retrieved from the Royal Meteorological Institute of Belgium, in near real-time with  
137 a latency of about 40 minutes. The ARG data were replaced by quality-controlled Edition 1 data  
138 produced by the GERB Ground Segment Processing System (GGSPS) after about 40 days  
139 [*Harries et al.*, 2005; *Dewitte et al.*, 2008]. Documentation on the GGSPS may be downloaded  
140 from <http://ggsps.rl.ac.uk/information.html#Publications>. The GERB instrument was turned off  
141 for periods of several hours or longer on 16 individual days in 2006 and for a longer period from  
142 24 September to 9 October, because of autonomous or commanded safety shutdowns. In addition,  
143 the instrument was routinely shut down for up to 6 hours around midnight during the eclipse  
144 seasons at the equinoxes, to prevent direct sunlight from damaging the detectors [*Harries et al.*,  
145 2005]. In 2006, these periods covered 9 February to 23 April and 18 August to 30 October.

146 All of the radiative fluxes shown here are daily means, which simplifies combining the ARM  
147 point measurements with the GERB area-average measurements. The averaging process removes  
148 the diurnal variability and the high frequency noise that arises from small-scale cloud features  
149 advecting over the AMF and through the GERB pixels. It also simplifies investigations of the  
150 influence of the meteorological changes on the fluxes and divergences over a timescale of days  
151 and longer, which is the primary focus of this work.

## 152 **2.2. Sources of error in the radiative fluxes and divergences**

153 The errors in the daily mean fluxes and divergences arise from three main sources, which are  
154 considered below. Combining these sources enables an estimate of the overall error to be made.

### 155 **2.2.1. AMF and GERB fluxes**

156 This source of error includes the instruments themselves and the processing of the measurements  
157 to produce fluxes. Uncertainties in the AMF fluxes are given by *Slingo et al.* [2006] as  $9.0 \text{ Wm}^{-2}$   
158 for the total downwelling shortwave, although this could be as large as  $25 \text{ Wm}^{-2}$  at the peak of  
159 the March 2006 dust storm, and  $5.1 \text{ Wm}^{-2}$  for the downwelling longwave. Estimates of the  
160 absolute accuracy of the GERB radiances are given by *Slingo et al.* [2006] as 2.25% in the  
161 shortwave and 0.96% in the longwave. They note that angular models introduce additional errors  
162 of  $10 \text{ Wm}^{-2}$  for typical shortwave fluxes and  $5 \text{ Wm}^{-2}$  for longwave fluxes, with the expectation  
163 that the latter will be an underestimate for aerosols, which are not (as yet) identified in the  
164 processing system. Results shown by *Bharmal et al.* [2008] are consistent with this conclusion.  
165 *Dewitte et al.* [2008] analyse comparisons between co-located GERB and CERES data and  
166 conclude that the GERB accuracy is 5% for reflected shortwave radiances and 2% for the emitted  
167 longwave radiances. For typical daily mean shortwave and longwave fluxes shown later of 100-  
168  $200 \text{ Wm}^{-2}$  and  $300 \text{ Wm}^{-2}$ , respectively, these numbers correspond to  $5\text{-}10 \text{ Wm}^{-2}$  and  $6 \text{ Wm}^{-2}$ ,  
169 consistent with the estimates from *Slingo et al.* [2006] quoted above.

### 170 **2.2.2. Interpolation across missing data**

171 The most serious source of missing data for the daily means is the shutdown of GERB during the  
172 eclipse seasons, with the loss of up to 6 hours of data every night. Shortwave data are also  
173 masked as unavailable during the sun-glint period of about one hour around 1130 local time. A  
174 simple linear interpolation of the data across these periods was applied. The impact was  
175 quantified by applying the interpolation to days when data were present and comparing the actual  
176 and interpolated daily means. For the interpolation at night, the impact on the OLR was  $-0.1 \pm 0.8$   
177  $\text{Wm}^{-2}$  for clear days and  $0.1 \pm 2.5 \text{ Wm}^{-2}$  for cloudy days. The small systematic component reflects  
178 the fact that the OLR typically changes quite slowly through the night, at least for clear skies, and  
179 this behavior is approximately linear [e.g., *Comer et al.*, 2007]. For the shortwave interpolation,  
180 the impact on the reflected shortwave was  $-5 \pm 5 \text{ Wm}^{-2}$  for clear days and  $-4 \pm 17 \text{ Wm}^{-2}$  for cloudy  
181 days. Extended periods during which GERB was turned off for other reasons could not be dealt

182 with in this way (notably 24 September to 9 October), so these days were excluded from the  
183 analysis altogether.

### 184 **2.2.3. Inhomogeneities and spatial sampling**

185 *Settle et al.* [2008] analyse the sampling errors that arise from using the AMF measurements at a  
186 single location to represent the surface radiation budget beneath GERB. For the shortwave fluxes,  
187 there is a systematic error from geographical variability of the surface albedo of about  $10 \text{ Wm}^{-2}$ ,  
188 and a random error, mainly from clouds, of about  $3 \text{ Wm}^{-2}$  in the dry seasons, rising to  $12 \text{ Wm}^{-2}$  at  
189 the peak of the wet season in August. For the longwave fluxes, there is a systematic error from  
190 geographical variability of the surface temperature of about  $4 \text{ Wm}^{-2}$  and a random error, mainly  
191 from clouds, of about  $3 \text{ Wm}^{-2}$ .

### 192 **2.2.4. Estimate of the errors in the divergences**

193 The divergences are calculated as the difference between the TOA and surface radiation budgets,  
194 so the errors discussed above are cumulative. In combining the errors, we make the usual  
195 assumption that the random errors from different instruments or observing systems are  
196 uncorrelated. In reality, there may be some correlation and it is rarely possible to be entirely sure  
197 how much of a stated error is systematic and how much random. These estimates hopefully err on  
198 the side of caution and should therefore be regarded as guidelines rather than definitive.

199 In the shortwave, we combine the GERB error of  $\pm 10 \text{ Wm}^{-2}$  with the AMF error of  $\pm 9 \text{ Wm}^{-2}$  for  
200 each of the two radiometers used to calculate the net flux at the surface, together with the  
201 interpolation and sampling errors mentioned above. The overall random error in the shortwave  
202 divergences is then  $\pm 16 \text{ Wm}^{-2}$  in the dry seasons and  $\pm 20 \text{ Wm}^{-2}$  in the wet season, with a  
203 systematic sampling error of about  $10 \text{ Wm}^{-2}$ . The random error is about 20% of the shortwave  
204 divergences shown later, which illustrates the difficulty in making definitive estimates of this  
205 quantity from observations.

206 In the longwave, the GERB error of  $\pm 6 \text{ Wm}^{-2}$  is combined with the AMF error of  $\pm 5.1 \text{ Wm}^{-2}$  for  
207 each radiometer and the sampling error of  $\pm 3 \text{ Wm}^{-2}$  to produce an estimate of the uncertainty in  
208 the longwave divergences of  $\pm 10 \text{ Wm}^{-2}$ , with a possible systematic error of about  $4 \text{ Wm}^{-2}$ . In this  
209 case, the random error is only about 6% of the longwave divergences shown later, which are thus  
210 known with much greater accuracy than the shortwave divergences. The comparisons shown by  
211 *Bharmal et al.* [2008] between divergences calculated from the data and from radiative transfer

212 simulations produce similar values, in support of these estimates.

### 213 **2.3. Clouds**

214 Two cloud masks are available for the analysis of the fluxes. The first is based on the operational  
215 CLMK cloud mask product generated by the Nowcasting Software Application Facility using  
216 SEVIRI (Spinning Enhanced Visible and Infrared Imager) data on Meteosat-8 [*Schmetz et al.*,  
217 2002]. This is available throughout the period from the EUMETSAT on-line archive  
218 (<http://archive.eumetsat.org>). The CLMK data are at the same spatial and temporal resolution as  
219 the SEVIRI imagery (3km and 15 minutes). They are derived from a higher-level cloud  
220 classification product, which uses a two step process to first identify clouds, and then classify  
221 them [*Derrien and Gléau*, 2005]. The cloud identification and classification processes both use a  
222 series of tests based on multi-spectral thresholds, where the threshold values are determined  
223 dynamically depending on illumination conditions and geographical location, climatological data,  
224 numerical weather prediction data and radiative transfer models. At night time only those tests  
225 that use the thermal infrared SEVIRI channels are available, with the result that the cloud  
226 classification is less reliable: for example, airborne dust is sometimes indistinguishable from low  
227 warm clouds. For the AMF Niamey airport and Banizoumbou sites, regions of 17 by 17 pixels  
228 (covering a GERB ARG pixel) centred on each site were extracted from the CLMK data, from  
229 which time series of top-of atmosphere estimates of cloud cover were generated.

230 A second cloud mask was derived from the cloud fractions retrieved by *Kollias et al.* [2008] from  
231 the W-band (95GHz) cloud radar, micropulse lidar and ceilometer at the main AMF airport site.  
232 These are vertically pointing instruments with narrow fields of view, so the cloud mask is only  
233 representative of the atmosphere directly over the Niamey airport site. Unfortunately, the data do  
234 not cover the entire year, because the cloud radar only became operational in mid-March. Daily  
235 mean cloud fractions were calculated as vertical means of the daily mean values at all levels from  
236 *Kollias et al.* [2008].

237 The results shown later were not particularly sensitive to which cloud mask was used to sample  
238 the data for clear and cloudy conditions. However, since the SEVIRI mask relates directly to the  
239 GERB footprint and is available for the whole year, it was decided to use this exclusively in this  
240 paper. A daily average of the cloud mask was created in order to provide a binary flag for  
241 conditionally sampling the radiation data, and days were flagged as cloudy if this average value

242 exceeded a threshold of 0.3.

## 243 **2.4. Aerosols**

244 Retrievals of aerosol optical thickness were obtained from the AERONET site at Banizoumbou,  
245 approximately 60km east of Niamey airport [Holben *et al.*, 2001]. The data from this site  
246 represent the most comprehensive and local retrievals that are available throughout the AMF  
247 deployment. A CIMEL sunphotometer, as used by AERONET, was also deployed at the AMF  
248 Niamey airport site, but was only present from August 2006 until the end of the deployment, so  
249 the Banizoumbou data are preferred here. The data used are the diurnally-averaged AERONET  
250 version 2 direct sun inversions of aerosol optical thickness at 870nm. These data have the  
251 advantage of being cloud screened with associated error estimates; the so-called Triplet Variance,  
252 from 3 measurements within 90 seconds. Turner [2008] also uses AERONET data from this site  
253 to compare with optical thicknesses retrieved from the AERI infra-red window radiances and  
254 confirms that the data correlate well with the infra-red optical thicknesses.

255

## 256 **3. Cloud and aerosol timeseries**

257 In this and the subsequent sections, the wet season is defined as in Part 1; from 5 May to 29  
258 October. The period before 5 May is referred to as the first dry season and that after 29 October  
259 as the second dry season.

### 260 **3.1. Clouds**

261 Figure 1a shows the mean cloud fractions derived from the SEVIRI cloud mask as the solid line.  
262 In the first dry season, cloud amounts were low, with mainly thin cirrus associated with the sub-  
263 tropical jet stream to the north or with convection to the south of Niamey, plus occasional thin  
264 mid-level clouds that formed at the top of the aerosol-laden boundary layer at around 5km  
265 altitude. Cloud amounts increased with the arrival of the wet season and most cloud occurred in  
266 July, August and September, associated with the summer monsoon. The early and late monsoon  
267 periods were relatively clear in comparison, probably due to the moist monsoon air layer being  
268 too shallow to support deep convection, although the onset and retreat of the monsoon were still  
269 apparent in the change in the amount and frequency of cloud. The summer monsoon brought in  
270 the moisture necessary to support deep, moist convection, and so summer cloud types were more

271 variable, consisting not only of thin cirrus, but also thicker low and mid-level convective cloud.  
272 After the retreat of the monsoon in October, cloud amounts returned to small amounts of cirrus,  
273 with fewer lower level clouds than in the first dry season.

274 The dashed line on Figure 1a shows the cloud fractions derived from the *Kollias et al.* [2008]  
275 data. These correlate well with the SEVIRI data, although the absolute amounts of cloud are not  
276 the same, because of differences between the fields of view of the satellite and AMF instruments  
277 and between the cloud detection algorithms.

### 278 **3.2. Aerosols**

279 Aerosol loadings were significant throughout the year (Figure 1b), with several major events in  
280 addition to the previously documented dust storm in early March [*Slingo et al.*, 2006]. Apart from  
281 these individual dust outbreaks, the background aerosol optical thickness remained at around 0.3  
282 for the first half of the year, falling gradually during the late summer monsoon period to around  
283 0.2, and reaching the lowest levels during the second dry season. The largest sustained values  
284 were in the wet season, particularly in June, when dust was raised by the gust fronts propagating  
285 away from deep convection. The reduction in background levels late in the monsoon may have  
286 been due to the wetting of the surface and the growth of vegetation following rainfall, both of  
287 which would have reduced the amount of dust available to be lifted by the wind. The lowest  
288 aerosol loadings occurred in the second dry season, providing good conditions for testing clear-  
289 sky radiation simulations [*Bharmal et al.*, 2008; *McFarlane et al.*, 2008].

290

### 291 **4. Radiative flux timeseries**

292 This section presents the radiative fluxes measured at the surface by the AMF and at the TOA by  
293 GERB. The fluxes are presented first as time series to show the variation over the course of the  
294 year, and are then shown plotted against the dominant influences on this variability to illustrate  
295 the main controls on the radiation fields. These influences include the cloud and aerosol data  
296 discussed in Section 3, plus the air temperature and column water vapor (CWV) data presented in  
297 Part 1. The CWV data used here are from the microwave radiometer, using the MWRRET  
298 algorithm (see Part 1 for details). Understanding the controls on the radiative fluxes is essential  
299 for interpreting the radiative divergence results, to be discussed in section 6, as the divergences  
300 are calculated from the component fluxes.

#### 301 **4.1. Surface longwave fluxes**

302 Figure 2 shows the surface downwelling, upwelling and net longwave radiative fluxes measured  
303 by the AMF at Niamey airport. Downwelling longwave radiation (DLR, Figure 2a) increased  
304 overall through the first dry season by about  $30 \text{ Wm}^{-2}$ , but periodic increases above the base level  
305 of over  $50 \text{ Wm}^{-2}$  occurred during this period, coinciding with dry season cloud and water vapour  
306 advection events, as well as the dust storm in early March. The onset of the monsoon can be seen  
307 clearly in mid April, when the DLR showed a sudden increase with the arrival of more humid air.  
308 This was referred to as a “false onset” in Part 1, as it was followed by a break, the main monsoon  
309 arriving only at the beginning of May. The DLR reached a maximum during the early part of the  
310 wet season, when the atmosphere was still relatively cloud free (Figure 1a), but very warm and  
311 humid. It then dropped by over  $20 \text{ Wm}^{-2}$  in the later and cloudier part of the monsoon, when the  
312 increased cloud cover and hence lower shortwave insolation (see below), coupled with greater  
313 evaporation from the surface [Miller *et al.*, 2008], led to lower surface and atmospheric  
314 temperatures. The end of the monsoon at the end of October was associated with a precipitous  
315 drop in the CWV (Part 1, Figure 8), which produced a corresponding reduction in the DLR of  
316 over  $50 \text{ Wm}^{-2}$ . In the second dry season, the strong signals from variations in CWV and in  
317 aerosol loadings (Figure 1b) are once again apparent. The lowest fluxes occurred at the end of the  
318 year, when the surface and air temperatures reached their minimum values (Part 1).

319 While the behavior of the downward thermal fluxes described above appears straightforward, it  
320 actually results from a very unusual combination of changes in temperature and humidity. As  
321 shown in Part 1, surface and air temperatures increased during the first dry season to a maximum  
322 at the start of the monsoon in May. Temperatures then decreased to the peak of the monsoon in  
323 August, recovered in September/October, before dropping steadily towards the end of the year. In  
324 contrast, near-surface humidities and the CWV decreased through the first dry season, then  
325 increased as the monsoon arrived and reached their highest values at the peak of the monsoon.  
326 They decreased in September/October and dropped to low values again at the end of the year.  
327 Apart from in the second dry season, the seasonal changes in temperature and humidity were thus  
328 out of phase with each other. The reason is that humidity variations in this region are controlled  
329 by the wind direction and by the origin of the airmass (and hence by the large-scale atmospheric  
330 dynamics) more than by the temperature. This aspect of the climatology of the region is well  
331 known, but the impact on the longwave radiative fluxes and divergences is remarkable, as

332 discussed later. As far as we are aware, this behavior has not been documented before.

333 The upwelling longwave radiation (Figure 2b) is determined by the surface temperature and  
334 emissivity, with changes in the latter being less important [Settle *et al.*, 2008]. The surface  
335 temperature was in general slightly higher than the air temperature, but the two were closely  
336 coupled, so that comparison of Figure 2b with the timeseries of air temperature (Figure 5, Part 1)  
337 shows that both the low and high frequency variations in the upward flux closely followed those  
338 of the temperature.

339 The net longwave radiation at the surface (Figure 2c) is also dependent on temperature, as is  
340 shown later, but the most consistent influence appears to be from the CWV, as may be seen by  
341 comparing with Figure 8 in Part 1. The largest net longwave thus occurred at the end of the first  
342 dry season, when the CWV was at its lowest value, which allowed the surface to cool more  
343 efficiently out to space. The net longwave dropped progressively through the wet season,  
344 reaching a minimum in August when the CWV reached its maximum. At this time, the  
345 atmosphere was at its most opaque and so the surface cooling was minimised. The net longwave  
346 increased again during the second dry season, as the CWV fell again. Cloud events always  
347 reduced the net longwave, particularly so during the dry seasons when the low CWV led to  
348 values of the cloud radiative effect that reached several tens of  $\text{Wm}^{-2}$ , even from the middle level  
349 and high clouds present at this time.

#### 350 **4.2. Surface shortwave fluxes**

351 The incoming shortwave radiation (Figure 3a) increased with the seasonal increase in insolation  
352 at the TOA through the first dry season until near the end of April, when the sun passed overhead  
353 at Niamey (Figure 4c). During the monsoon, solar radiation received at the surface decreased  
354 substantially, mainly because of the increased cloudiness but also, as will be shown later, because  
355 of water vapor absorption. The incoming shortwave was thus lower when the sun passed  
356 overhead for the second time in late August, compared with April, and continued to decrease  
357 thereafter as the sun moved further south. Comparison with Figure 1 shows that both clouds and  
358 aerosol caused large reductions all year round from the clear sky values, but that these became  
359 more frequent in the wet season, particularly during the cloud maximum between July and  
360 September. The impact of the dust storms evident in Figure 1b, such as that in early March and  
361 the extended feature in mid-June, can also be seen clearly. These are the main causes of reduced

362 solar transmission to the surface during the dry season, apart from the impact of two cloud events  
363 during the first dry season. The onset and retreat of the monsoon were not so clearly marked in  
364 the solar than in the thermal, and the retreat appeared to occur almost a month sooner. This is  
365 because the main effect of the monsoon on solar fluxes is the impact of cloud, with a smaller  
366 impact of humidity. In the thermal region, the humidity of the monsoon air layer is much more  
367 important. The build up of monsoon cloud happened gradually, whereas the arrival of the  
368 monsoon air brings a sudden change in water vapour content. In addition, the area of convection  
369 moves south sooner than the moist air layer since it becomes shallower towards the north,  
370 therefore becoming too shallow to support cloud late in the monsoon season.

371 The reflected shortwave radiation at the surface (Figure 3b) shows the same basic pattern, with  
372 the additional effect of changes in the surface albedo [McFarlane *et al.*, 2008]. The reduction in  
373 albedo during the wet season due to the higher average sun angle and the darkening of the surface  
374 due to rainfall and vegetation growth reduced the reflection at this time, amplifying the seasonal  
375 changes seen in the incoming shortwave.

376 The net shortwave (Figure 3c) shows that the absorption of solar radiation by the surface was a  
377 maximum in the early period of the wet season, but was reduced substantially by cloud from July  
378 through September. This reduction in the insolation drove the drop in surface and air  
379 temperatures through the monsoon, documented in Part 1. The signals of dust events and of cloud  
380 at all times of the year, apparent in the component fluxes, can also be seen in the net radiation.

### 381 **4.3. Top of atmosphere fluxes measured by GERB**

382 Figure 4a shows that the OLR increased during the first dry season and then dropped by over 50  
383  $\text{Wm}^{-2}$  as the monsoon developed, recovering during the second dry season. These changes were  
384 driven in part by the same temperature and humidity variations discussed above. The OLR is  
385 most sensitive to humidity changes in the mid and upper troposphere, but Figure 8b in Part 1  
386 shows that these changes were correlated with changes in the CWV, which is used here. In the  
387 case of the OLR, these variations mostly acted in the same direction, so that OLR increased both  
388 because of increasing temperature and of decreasing CWV during the first dry season, and  
389 similarly decreased in the wet season as the CWV increased and the surface and lower  
390 tropospheric temperatures fell. This picture is complicated by clouds and to a lesser extent  
391 aerosol outbreaks, both of which acted to reduce the OLR. The cloud effect is apparent

392 throughout the year, although the deep convective cloudiness during the monsoon consistently  
393 produced the lowest OLR values. Following the monsoon retreat, OLR rose as the atmosphere  
394 again became more transparent to thermal radiation. Towards the end of the year, several  
395 exceptionally clear and dry periods allowed the OLR to rise, countering the effect of the fall in  
396 surface temperature.

397 The annual variation in the reflected solar radiation at the TOA (Figure 4b) is controlled by the  
398 insolation (Figure 4c), which was a minimum at the beginning of the year when the sun was  
399 furthest south and a maximum when the sun passed overhead in late April. The main cause of  
400 short-term albedo increases was the presence of bright, thick cloud. This caused large increases in  
401 reflection above the baseline curve, particularly in the later, cloudier phase of the monsoon when  
402 bright monsoon weather systems passed over the AMF site frequently, but also on one occasion  
403 in late January when unusually thick cloud was present.

404

## 405 **5. Radiative flux scatter plots**

406 The discussion in the previous section shows that several relationships are apparent between the  
407 radiative fluxes and the meteorology from comparisons of the temporal variations. However, it is  
408 possible to look more closely at these relationships by plotting the radiation data against their  
409 controlling meteorological variables, and thereby gain more insight into the behavior of the  
410 fluxes that determine the radiative divergences. The longwave radiative fluxes are discussed first,  
411 followed by the shortwave.

### 412 **5.1. Longwave scatter plots**

413 In Section 4.1, it was argued that temperature and CWV have opposing influences on the DLR at  
414 the surface. In this section, these influences are examined further, with guidance from the simple  
415 formula developed by *Prata* [1996], which parametrizes the clear-sky DLR in terms of these two  
416 variables. Prata's formula is based on an analytic approximation to represent the dependence of  
417 the effective emissivity of the atmosphere on the CWV. In the paper, it was tested using both  
418 radiative transfer calculations and datasets of simultaneous measurements of air temperature,  
419 vapor pressure and DLR. The formula reproduces the dependence of the clear-sky DLR on  
420 temperature and CWV found in various global datasets [*Allan*, 2006], and it therefore provides a  
421 useful background for the analysis of the Niamey data.

422 Prata's formula for the DLR at the surface may be written as

$$423 \quad \text{DLR} = \varepsilon \sigma T^4, \quad (1)$$

424 where  $\sigma$  is the Stefan-Boltzmann constant and  $T$  is the screen-level temperature. The effective  
425 emissivity of the atmosphere  $\varepsilon$  is approximated as

$$426 \quad \varepsilon \approx 1 - (1 + u) \cdot \exp\{- (1.2 + 3.0 u)^{0.5}\}, \quad (2)$$

427 where  $u$  is the CWV in units of  $\text{g cm}^{-2}$ . The values of the DLR are thus calculated from two  
428 variables, the screen-level temperature  $T$  and the column water vapour  $u$ .

429 The symbols on the upper panels of Figures 5 and 6 show the values of the daily mean DLR  
430 measured at the Niamey airport site scatter-plotted against the observed screen-level  $T$  (Figure 5)  
431 and against the observed CWV (Figure 6). The symbols are colored according to whether the  
432 observations were made during the dry or wet seasons. In addition, the dotted lines show the  
433 values of DLR predicted by equations 1 and 2, where in each plot the dependence on either  $T$  or  
434 CWV is shown for several fixed values of the other input variable. This provides a series of  
435 idealized "Prata curves" that illustrate the dependence of the DLR on only one variable, with the  
436 other held constant. They should not be interpreted as simulations of the actual data points, but  
437 merely as an aid to the analysis below. When the Prata formula is provided with both of the  
438 observed values of  $T$  and CWV, the simulated fluxes agree quite well with the data, as was  
439 shown in the analysis of the March 2006 dust storm [*Slingo et al.*, 2006, Figure 3].

440 The lower panels in Figures 5 and 6 show simplified versions of the trajectories of the observed  
441 values of the DLR through the year, which summarise the seasonal variations of the observations  
442 and their dependence on  $T$  and CWV.

443 Figure 5 shows that the DLR increases with air temperature, as expected, but two complications  
444 are apparent. Firstly, the wet season fluxes are much higher than those during the dry season at  
445 the same air temperature, because the CWV (and hence the effective emissivity of the  
446 atmosphere) was much larger at this time of year. Secondly, the slope of the wet season fluxes is  
447 much lower than that during the dry season and the data points cross the Prata curves. This is  
448 because the lowest temperatures occurred in August, when the CWV was a maximum, whereas  
449 the highest temperatures in May were associated with somewhat lower CWV, as noted earlier. In  
450 addition, there was much more cloud late in the season, which further increased the emission to

451 the surface at that time. Taken together, these factors lead to a much lower slope in the wet  
452 season, as the data points move across the Prata curves for constant values of CWV.

453 The lower panel in Figure 5 illustrates the trajectory of the data points. At the beginning of the  
454 year, temperatures were around 25 °C and increased through the first dry season to around 35 °C  
455 whilst the DLR points moved onto a slightly lower Prata curve. With the monsoon onset,  
456 temperatures remained high but the DLR points jumped up to the 4 cm CWV Prata curve, after  
457 which the temperatures decreased. In late summer, the CWV was at its highest, but the  
458 temperature continued to fall, moving the DLR down the highest Prata curve. After the monsoon  
459 retreat, the temperature returned to around 30 °C, but the CWV fell, moving the DLR back to the  
460 lower Prata curves. As the year came to an end, the falling temperatures and CWV brought the  
461 DLR to its lowest values by moving it down more steeply than predicted by the idealized Prata  
462 formula. Cloud had additional effects on the DLR, but did not change this basic result.

463 The dependence of the DLR on CWV is illustrated in Figure 6. The Prata equations predict that  
464 the effective emissivity of the atmosphere and hence the DLR should increase with CWV. This is  
465 broadly true for the data points, but again these cluster into separate groups for the two seasons.  
466 In this plot, the trajectory of the points is very different in the two dry seasons, as shown in the  
467 lower panel. During the first dry season from January to April, air temperatures increased by  
468 approximately 10 °C as the CWV decreased, moving the DLR onto progressively higher Prata  
469 curves but *backwards* on the CWV axis. With the monsoon onset, temperatures remained high,  
470 so the DLR followed the highest Prata curve in the direction of increased CWV, reaching about 4  
471 cm in May. Thereafter, despite steadily increasing CWV, the DLR dropped as temperatures fell,  
472 moving the points onto a lower Prata curve in August. Following the monsoon retreat in October,  
473 the DLR dropped suddenly as both temperature and CWV fell, moving the data points to their  
474 lowest values and following a trajectory very different from that in the first dry season, but more  
475 in line with that predicted by the Prata formula.

476 Figures 5 and 6 provide valuable insights into how the opposing influences of changes in  
477 temperature and CWV led to the observed seasonal changes in the DLR. A similar analysis is  
478 now applied to the net longwave radiation at the surface and to the OLR, providing further  
479 background for the divergences presented in Section 6 and for the analysis in Section 7, in which

480 the effects on the radiative divergences are interpreted within the framework of a simple model of  
481 the greenhouse effect.

482 Figure 7 shows scatter plots of the net longwave radiation at the surface against temperature and  
483 CWV. The effect of the very different behavior of the DLR in the dry and wet seasons seen in  
484 Figure 5a is apparent in Figure 7a. In the dry seasons, the dependence of the DLR on temperature  
485 shown in Figure 5a roughly follows the Prata curves, with the result that the net radiation  
486 becomes only slightly more negative as the air temperature increases (Figure 7a). In contrast, the  
487 very different slope in the wet season seen in Figure 5a translates into a strong increase of the  
488 surface longwave cooling with temperature. The cooling is largest at the start of the wet season,  
489 when temperatures are highest but the CWV is still relatively low, and is lowest in August when  
490 temperatures have dropped but the atmosphere is at its most opaque (see also Figure 2c).

491 The difference between the dry and wet seasons is less apparent when the net longwave radiation  
492 is plotted against CWV (Figure 7b), as was also the case with the DLR. Here, the behavior is  
493 very much as expected, despite the scatter, with a steady reduction in the surface cooling as the  
494 CWV increases and the smallest values associated with cloudy days during the wet season.

495 The final component of the longwave radiation budget is the OLR, scatter plots for which are  
496 shown in Figure 8. The dependence on the screen-level air temperature is weak, with  
497 considerable scatter, particularly in the wet season when the atmosphere was more cloudy (Figure  
498 8a), but there is some evidence of an increase in OLR with air temperature that is most apparent  
499 in the dry season. The isolated group of points with the highest values of OLR correspond to  
500 early April, just before the false monsoon onset, when the CWV was smallest and so the  
501 transmission of the surface emission to space was at a maximum.

502 Figure 8b also shows considerable scatter, but it does demonstrate that OLR decreases with  
503 increasing column water vapour, as would be expected if changes in the mid and upper  
504 tropospheric humidity to which the OLR is most sensitive occur in synchronism with those at  
505 lower levels, which appears to be the case (cf Figure 8b in Part 1). While it would be difficult to  
506 fit a reliable trend line through these data, it is important to note that the dependence of the OLR  
507 on CWV is roughly a mirror image of that for the surface net longwave shown in Figure 7b. This  
508 implies that the rate at which the atmosphere increases its net emission to the surface as CWV  
509 increases is roughly matched by the rate at which it traps the OLR. This compensation between

510 the dependence of the surface net longwave and of the OLR on the CWV provides the key to  
511 understanding the behavior of the atmospheric longwave divergence, as is shown later.

512 In many other environments of the world, one would not expect to find a significant dependence  
513 of the longwave fluxes on aerosol loadings, either because the mass loadings are too low or  
514 because the aerosol is too small to have an appreciable impact on thermal radiation. However, in  
515 the Sahel, where Niamey is located, the impact can be large [e.g., *Slingo et al.*, 2006]. To  
516 investigate this, Figure 9 shows scatter plots of the DLR at the surface and of the OLR against the  
517 aerosol extinction, defined as

$$518 \quad \text{extinction} = 1 - \exp(-\tau), \quad (3)$$

519 where  $\tau$  is the aerosol optical thickness at 870nm from the Banizoumbou AERONET site.  
520 Extinction is used here because of the large range of values of optical thickness encountered  
521 through the year. Figure 9a shows that there is a measurable dependence of the DLR at the  
522 surface on aerosol, at least in the dry season when the effective emissivity of the atmosphere is  
523 low. In the wet season, the dependence is masked by the much larger changes in the other  
524 variables. The OLR is less sensitive, which is to be expected as the aerosol is mainly found in the  
525 lowest layers of the atmosphere. For comparison, the dotted lines show the fluxes computed by  
526 *Turner* [2008] for aerosol spheres consisting of Kaolinite (the most common mineral found in his  
527 retrievals), embedded in an atmospheric profile typical of the first dry season. The 11 micron  
528 optical thicknesses used by *Turner* [2008] were converted to the values of the extinction at  
529 870nm shown in Figure 9 using an assumed Angstrom coefficient of 0.326, which *Turner* [2008]  
530 obtained when he compared his retrievals with the Banizoumbou AERONET data at 1.02  
531 microns. Figure 9 shows that the shapes of the simulated curves fit the data well, although the  
532 simulations are somewhat lower than the observed fluxes.

## 533 **5.2. Shortwave scatter plots**

534 The main factors that control the shortwave fluxes are more apparent in the timeseries than is the  
535 case for the longwave fluxes, as was shown in Section 4. For example, the modulation of the  
536 fluxes by the incoming solar radiation at the TOA and the signals of clouds and major aerosol  
537 events are very clear in Figures 3 and 4. One complication is the significant seasonal variation in  
538 the surface albedo [*McFarlane et al.*, 2008], which was highest in the dry season and lowest in  
539 the wet season as the surface became wetter and vegetation grew [*Settle et al.*, 2008]. Another

540 complication is scattering by aerosols and clouds, which makes it difficult to perform as simple  
 541 an analysis for the individual fluxes as in the longwave. Nevertheless, a few scatter plots are used  
 542 here to illustrate the effects of the CWV and aerosol loadings in the shortwave. In these plots, the  
 543 daily fluxes are normalized by the value of the insolation at the TOA on that day. To first order,  
 544 this removes the external astronomical control on the solar fluxes, leaving the meteorological  
 545 controls to show their influence more clearly in the scatter plots. The normalized downward  
 546 shortwave radiative flux at the surface thus becomes the effective solar transmittance and the  
 547 normalized reflected shortwave flux at the TOA becomes the albedo.

548 Figure 10a shows a scatter plot of the normalized downwelling shortwave flux at the surface (i.e.  
 549 the transmittance) against the CWV. The distribution of points is highly skewed, with low values  
 550 mainly due to cloud but also to aerosol events. However, the upper envelope of the points follows  
 551 a clear trend downwards with increasing CWV. This trend is due to water vapor absorption, as  
 552 may be seen by comparing the points with the dotted line, which shows the broadband  
 553 transmittance predicted by the modified Lacis-Hansen scheme developed by *Ramaswamy and*  
 554 *Freidenreich* [1992, their Section 2 and Table 2]. This line takes no account of scattering, either  
 555 within the atmosphere or from the surface, but it does illustrate that the trend of the observations  
 556 is consistent with increasing amounts of water vapor absorption.

557 The corresponding scatter plot against the aerosol extinction at 870nm, for clear skies only, is  
 558 shown in Figure 10b. The data points again follow a downward trend and two curves are also  
 559 plotted to assist the interpretation. The first shows a linear fit to the transmittance as a function of  
 560 the aerosol optical thickness obtained by *McFarlane et al.* [2008, their Figure 11];

$$561 \quad T_1 = 1 - 0.12 * \tau, \quad (4)$$

562 where  $\tau$  is the optical thickness at 523nm, which has been adjusted to the value at 870nm for  
 563 plotting on Figure 10b using the same Angstrom coefficient as in the previous section.

564 The second curve is given by the analytical expression from the two-stream equations for the  
 565 transmittance of a slab composed of conservative scatterers (i.e. the single scatter albedo is 1);

$$566 \quad T_2 = 1 - (1-f) * \tau / \{1 + (1-f) * \tau\}, \quad (5)$$

567 where  $f$  is the fraction of the radiation that is forward scattered in a single event, given by  $(1-f) =$   
 568  $(1-g)/2$ , where  $g$  is the asymmetry parameter. *McFarlane et al.* [2008] retrieved a mean value of

569 0.67 for  $g$ , giving  $f=0.835$ , which is used in Equation 5.

570 The two curves are in good agreement with each other and are consistent with the trend of the  
571 data, except that most of the data points lie below the two curves at low values of the extinction  
572 (low optical thickness), particularly during the wet season. This is probably due to the fact that  
573 such clear conditions tend to be associated with higher values of the CWV, which Figure 10a  
574 shows will tend to have lower transmittances as a result of absorption by water vapor.

575 Finally, Figure 11 shows similar plots for the albedo at the TOA (calculated by normalizing the  
576 reflected shortwave flux measured by GERB by the calculated incoming shortwave flux), as a  
577 function of CWV and aerosol extinction. Figure 11a shows a negative relationship between the  
578 albedo and the CWV, although at higher water vapor loadings the atmosphere is more frequently  
579 cloudy, which greatly increases the albedo. The magnitude of the trend is consistent with that in  
580 Figure 10a, suggesting the impact of water vapor absorption, but seasonal changes in the surface  
581 albedo may also be contributing, since the highest albedo occurs in the dry season and the lowest  
582 at the end of the wet season.

583 Figure 11b shows no clear dependence of the TOA albedo on the aerosol extinction at low values,  
584 but there is a marked trend towards higher albedos for extinctions above about 0.5 (optical  
585 thicknesses above 0.69). The data point on the extreme right is for 8 March, during the major dust  
586 storm, when the albedo was enhanced considerably by the dust [*Slingo et al.*, 2006]. The other  
587 points on the right all correspond to significant dust events, which may also be seen by  
588 comparing Figure 1b with the reflected shortwave flux shown in Figure 4b. As with Figure 11a,  
589 there is a separation between the data points for the two seasons, which again points to an  
590 additional influence from changes in the surface albedo. Some data points that are well above the  
591 general trend are associated with days when the cloud mask failed to identify significant amounts  
592 of cloud that had a large impact on the GERB shortwave fluxes.

593

## 594 **6. Radiative divergences**

595 Having analyzed the component fluxes and discussed the factors that control them, this section  
596 presents estimates of the longwave, shortwave and net radiative divergences, obtained by  
597 combining the ARM surface data with the GERB data from space. This realizes one of the major  
598 goals of the RADAGAST project. Divergence is defined as the net radiation into a level, so that

599 positive values imply heating and negative values imply cooling. Surface divergence is therefore  
600 defined as the downwelling minus the upwelling radiation, corresponding to the net radiation into  
601 the surface. The TOA divergence is defined as the incoming minus outgoing radiation, i.e. the net  
602 radiation into the system. The atmospheric divergences are obtained by subtracting those at the  
603 surface from those at the TOA. The sign convention means that the longwave divergences are all  
604 negative, corresponding to cooling, while the shortwave divergences are all positive,  
605 corresponding to heating. The net divergences are obtained by adding the shortwave and  
606 longwave components. Although some of the surface and TOA divergences have already been  
607 discussed in earlier sections (e.g. the OLR), plots are also shown here, not only for completeness  
608 but also to illustrate how their behavior determines that of the atmospheric divergences.

### 609 **6.1. Timeseries of divergences**

610 Figure 12 shows the daily mean longwave radiative divergences through the year. As was found  
611 earlier, the seasonal variations in the TOA and surface divergences follow a very similar pattern,  
612 with maximum cooling both from the surface and out to space at the end of the first dry season,  
613 when temperatures were highest and the CWV (and hence the atmospheric emissivity) at a  
614 minimum. In contrast, the high values of CWV in August lead to the smallest values of the  
615 surface cooling and also the lowest values of the OLR. The effects at the TOA are strengthened  
616 by the cloudiness maximum at this time of year, although clouds also had a significant impact in  
617 the dry seasons.

618 The most remarkable feature in Figure 12 is the atmospheric divergence, which shows a much  
619 smaller variation through the year than the divergences at the TOA and at the surface. The small  
620 magnitude of this variation shows that most of the change in cooling at the TOA was made up of  
621 changes taking place at the surface, rather than in the atmosphere. From previous work (e.g.  
622 Stephens et al. 1994), one would expect the longwave cooling of the atmosphere to increase with  
623 the CWV, which does vary over a very large range in Niamey. However, while Figure 12 shows  
624 slightly higher cooling during the wet season than in the dry season, the magnitude of the  
625 difference is small. The reasons for this behavior are explored below.

626 Figure 13 shows the corresponding divergences in the shortwave. The upper envelope of these  
627 curves is clearly controlled by the seasonal variation in the daily mean insolation at the TOA  
628 (compare with Figure 4c). As in the longwave, the shortwave divergences at the TOA and at the

629 surface follow each other through the year, while the atmospheric divergence shows a smaller  
630 variation, although in the second dry season all three divergences show the same decline. Clouds  
631 produce the largest short term signals, but the magnitudes at the TOA and at the surface are  
632 similar, so that the effect of clouds tends to cancel in the atmospheric absorption, consistent with  
633 the expectation that clouds do not make a major contribution to atmospheric absorption in the  
634 shortwave. In contrast, comparison of Figure 13 with Figure 1b shows that aerosol events impact  
635 the surface divergence more than at the TOA, so that peaks in the atmospheric heating coincide  
636 closely with peaks in aerosol optical thickness. The decline in the atmospheric divergence  
637 through the second dry season is a result of the lower CWV and the generally lower aerosol  
638 loadings. In this season, the correspondence between the peaks in the divergence and the aerosol  
639 events seen in Figure 1b is particularly striking.

## 640 **6.2. Scatter plots**

641 It was shown in Section 5 that the effects of temperature and CWV have opposing influences on  
642 the DLR and net longwave radiation at the surface, and also on the OLR. The dependence on  
643 temperature was quite complicated, with different behaviors in the dry and wet seasons. The  
644 dependence on CWV was broadly as would be expected: a reduction in both the surface and TOA  
645 cooling with increasing CWV. Consistent with these results, Figure 14 appears to show no  
646 discernible dependence of the atmospheric longwave divergence on temperature, but a weak  
647 dependence on the CWV. Unfortunately, given the strong negative correlation between  
648 temperature and CWV, it is very difficult to interpret these scatter plots further, because they do  
649 not allow the two effects to be separated. A methodology that allows such a separation and which  
650 explains the behavior shown in Figure 12 is introduced in Section 7.

651 While scatter plots cannot unravel the dependence of the longwave divergence on temperature  
652 and CWV, they are valuable for other variables. The dependence of the atmospheric longwave  
653 divergence on the aerosol extinction is shown in Figure 15. This shows a discernible trend  
654 towards greater longwave cooling as the aerosol loading increases, consistent with the results in  
655 Figure 9, which show that the downward longwave at the surface is more sensitive to aerosol  
656 than the OLR. This dependence is somewhat stronger in the dry seasons.

657 The atmospheric divergence in the shortwave clearly increases with CWV, particularly at the  
658 lowest humidities (Figure 16a). The shortwave absorption also increases with the aerosol loading

659 (Figure 16b). This is mainly due to the reduced transmission to the surface (Figure 10b), because  
660 the TOA albedo actually shows an increase with the aerosol loading (Figure 11b), a characteristic  
661 feature of weakly absorbing aerosols.

662 Figure 17 shows that, over the course of the year, there is a small positive net gain of radiative  
663 energy at the TOA. The net radiation varies between the seasons, with the region gaining energy  
664 during boreal summer and experiencing a net energy loss during boreal winter. However, the  
665 surface gains radiative energy at all times of the year, but particularly during the summer  
666 monsoon, whilst the atmosphere continually loses radiative energy to space and to the surface at a  
667 steady rate of about  $75 \text{ Wm}^{-2}$ , increasing in the second dry season.

668 Table 1 summarises the annual means of all the daily mean fluxes and divergences, as well as  
669 their maximum and minimum values. No attempt has been made to interpolate over the extended  
670 periods when the GERB instrument was turned off (see Section 2.2.2). Together with the surface  
671 turbulent fluxes presented by *Miller et al.* [2008], this table provides a complete description of  
672 the annual means of the vertical flux terms at the AMF Niamey airport site during 2006.

673

## 674 **7. Interpretation of the longwave fluxes and divergences using a simple model**

675 One of the most remarkable results from this study is the compensation between the effects of  
676 changes in temperature and column water vapor on the longwave fluxes and atmospheric  
677 divergences. These changes are negatively correlated for much of the year, so the scatter plots do  
678 not allow the effects to be separated unequivocally from each other. In this section, we examine  
679 this result further and provide such a separation with the help of a simple model of the  
680 greenhouse effect. This employs a version of the methodology of *Stephens et al.* [1994].

681 Let the longwave atmospheric flux divergence be denoted by  $\Delta F$ . *Stephens et al.* [1994] write this  
682 in terms of the component fluxes as

$$683 \quad \Delta F = \sigma T_s^4 - F_\infty - F_g, \quad (6)$$

684 where the first term is the upward longwave flux from the surface, the second term is the  
685 outgoing longwave radiation (OLR) and the third term is the DLR at the surface.

686 The problem with (6) in this form is that the second and third terms depend both on temperature  
687 and on the atmospheric emissivity (which for clear-skies is largely controlled by the water vapor

688 profile). To deal with this, *Stephens et al.* [1994] introduced two dimensionless parameters that  
 689 normalize these two fluxes. Their choice of normalization was motivated by the desire to use  
 690 observed quantities (in their case  $\sigma T_s^4$  and OLR) to estimate the surface fluxes and atmospheric  
 691 divergence from readily available global sea surface temperature and OLR datasets. Here, since  
 692 the main purpose is to separate the effects of temperature and column water vapor, we choose  
 693 different normalizations that simplify the subsequent interpretation.

694 The first dimensionless parameter is the normalized greenhouse effect,  $G$ , defined here as

$$695 \quad G = F_\infty / \sigma T_s^4 \quad . \quad (7)$$

696 This is always smaller than unity in Niamey, reflecting the fact that the greenhouse effect acts to  
 697 reduce the emission to space, compared with that from the surface.

698 Similarly, the second dimensionless parameter is defined as

$$699 \quad F = F_g / \sigma T_s^4 \quad . \quad (8)$$

700 This is also smaller than unity, because the downward longwave radiation from the atmosphere is  
 701 always lower than the emission from the surface in Niamey. Comparison with Equation 1 shows  
 702 that  $F$  is equivalent to  $\epsilon$  in the Prata formula.

703 Substituting 7 and 8 into 6 leads to

$$704 \quad \Delta F = \sigma T_s^4 (1 - G - F), \quad (9)$$

705 where the value of  $\Delta F$  is generally negative, because on average the net effect of longwave  
 706 radiation is to cool the atmosphere.

707 To first order, Equation 9 separates the effects of temperature (the first term) from those of  
 708 atmospheric emissivity (the term in parentheses), although this is only approximate as in reality  
 709 both  $F_\infty$  and  $F_g$  depend on the full vertical profiles of both temperature and humidity.

710 The study by *Stephens et al.* [1994] concentrated on clear-sky data over the oceans. They showed  
 711 that the magnitudes of the greenhouse effect and of the clear-sky atmospheric longwave cooling  
 712 increased with both sea surface temperature and column water vapor. This behavior is largely  
 713 controlled by the Clausius-Clapeyron equation: over the oceans, the column water vapor (and  
 714 hence the effective emissivity of the atmosphere) is lowest at cold, high latitudes and highest at  
 715 warm, low latitudes. As a result, column water vapor and temperature are positively correlated

716 when global data are considered, as shown by *Stephens* [1990]. In contrast, over Niamey the  
717 column water vapor is controlled much less by the air temperature than by the atmospheric  
718 dynamics, so that the lowest values occur when the hot, dry Harmattan wind blows from the  
719 deserts, while the highest values occur during the wet season, when the air blows from the Gulf  
720 of Guinea. The net effect is that temperature and column water vapor are negatively correlated  
721 for most of the year, leading to the unusual impact on the longwave fluxes and heating rates  
722 found in this study.

723 To illustrate the impact on the longwave atmospheric divergence, scatter plots of  $G$ ,  $F$  and  $1-G-F$   
724 against CWV are shown in Figure 18. Although there is some scatter, this figure demonstrates  
725 that the dependence on the CWV of the normalized greenhouse effect and of the atmospheric  
726 emissivity seen from the surface are virtually mirror images of each other, so that the  $1-G-F$  term  
727 in Equation 9 is almost independent of CWV. As the CWV increases, the atmosphere thus loses  
728 longwave radiation to the surface with the same increasing efficiency with which it traps the  
729 OLR. The timeseries of these terms shown in Figure 19 illustrates the compensation between  $G$   
730 and  $F$  through the year and the approximate constancy of  $1-G-F$ . The remarkably small variation  
731 in the atmospheric longwave divergence through the year is thus due to the approximate  
732 cancellation between the normalized greenhouse effect  $G$  and the atmospheric emissivity seen  
733 from the surface  $F$ , which removes most of the dependence of the atmospheric cooling on the  
734 CWV, so that the remaining variations through the year of the divergence come from the  
735 relatively smaller changes in the  $\sigma T_s^4$  and  $1-G-F$  terms in Equation 9.

736

## 737 **8. Discussion and conclusions**

738 This paper has presented the broadband shortwave and longwave radiative fluxes measured from  
739 space and from the AMF site at Niamey airport during the RADAGAST experiment in 2006. The  
740 fluxes at the TOA and at the surface were combined to provide estimates of the divergence of  
741 radiation across the atmosphere. The radiation data were interpreted with the help of the surface  
742 air temperature and CWV data presented in Part 1, together with additional information on the  
743 cloud cover and aerosol optical depths from other datasets. These data were used to investigate  
744 the factors that control the radiative fluxes and divergences. The shortwave fluxes are controlled  
745 by the annual cycle of the insolation at the top of the atmosphere, by clouds, aerosols and water

746 vapor and by seasonal changes in the surface albedo. While clouds strongly influence the fluxes,  
747 their effect on the atmospheric shortwave divergence is much smaller. The longwave fluxes are  
748 controlled by the surface temperature, atmospheric temperatures, humidities and clouds and also  
749 by aerosols, which is a result of the unusually high loadings of dust aerosols present throughout  
750 the year. A remarkable compensation was found between the influence of the air temperature and  
751 CWV on the longwave fluxes, which was interpreted with the aid of the simple model of *Prata*  
752 [1996]. In addition, the atmospheric longwave divergence was found to be surprisingly constant  
753 through the year. A simple model of the greenhouse effect, based on the work of *Stephens et al.*  
754 [1994], provided helpful insights that suggested that this result is due to a cancellation between  
755 the dependence of the greenhouse effect seen from space and from the surface on the CWV.

756 There are several issues arising from this work that merit further investigation. The lack of  
757 sensitivity of the atmospheric longwave divergence to the large changes in CWV that take place  
758 through the year appears to be related to changes in humidity that are correlated through the  
759 whole depth of the troposphere, particularly during the wet season, as suggested by Figure 8b in  
760 Part 1. In the present paper, CWV is used as a surrogate for the changes in mid and upper  
761 tropospheric humidities, but more work is needed to quantify this relationship. A more detailed  
762 analysis of the sonde humidities is certainly required, coupled with controlled numerical  
763 experiments with radiation codes.

764 Clearly, it is also important to establish whether these results are unique to 2006 and how  
765 representative they are of the wider area beyond Niamey. Unfortunately, the paucity of surface  
766 radiative flux data in this region outside of the period when the AMF was deployed in Niamey  
767 means that the particular approach taken here would not be possible. However, it would be  
768 interesting to see whether numerical weather prediction (NWP) analyses, or re-analyses, might be  
769 used to investigate some of these issues. For example, the analyses could be evaluated against the  
770 RADAGAST data for 2006 to establish their strengths and weaknesses and then used to  
771 investigate other years and the applicability of the results to a wider geographical region. One  
772 limitation is that most NWP analyses do not explicitly include aerosols, some representation of  
773 which is clearly necessary. The analyses could also provide estimates of the atmospheric heat  
774 transport that must balance the non-zero net radiation at the top of the atmosphere shown in Table  
775 1. It would also be interesting to determine whether climate models can reproduce the radiative  
776 climatology found here, as well as the relationships between the radiative and other variables.

777 No attempt has been made here to derive information on the vertical profiles of the radiative  
778 divergences, but in principle techniques that use data from instruments at the permanent ARM  
779 sites [e.g., *McFarlane et al.*, 2007] could be applied to the RADAGAST data. This would also  
780 complement the investigation of mid and upper tropospheric humidities mentioned above.

781 Further analysis of the small impact of clouds on the atmospheric shortwave divergence found  
782 here would also be valuable, in view of the continuing uncertainty as to the existence of excess or  
783 anomalous cloud absorption [*Ramana et al.*, 2007]. It would certainly be interesting to see  
784 whether the RADAGAST data could be used to establish limits on the magnitude of any  
785 absorption that could not be reproduced by contemporary radiation codes, although the  
786 significant relative error found in Section 2.2.4 would clearly be a restriction.

787

788 **Acknowledgments.** We thank Didier Tanré for his efforts in establishing and maintaining the  
789 Banizoumbou AERONET site. The AMF data were obtained by the Atmospheric Radiation  
790 Measurement (ARM) Program, which is funded by the Office of Biological and Environmental  
791 Research, Office of Science, U.S. Department of Energy. Edition 1 GERB data were obtained  
792 from the GERB Ground Segment Processing System (GGSPS) at the Rutherford Appleton  
793 Laboratory, UK. We thank Richard Allan and David Turner for their comments on the  
794 manuscript. The analysis in Section 5.1 builds on the work of Peter Henderson for his PhD at  
795 ESSC, awarded in 2006. Anthony Slingo is supported by the National Centre for Earth  
796 Observation of the UK Natural Environment Research Council (NERC) and Gary Robinson is  
797 also supported by NERC. Helen White is funded by a NERC studentship and Nazim Ali Bharmal  
798 by NERC grant number NE/D002370/1.

799 **References**

- 800 Allan, R. P., 2006. Variability in clear-sky longwave radiative cooling of the atmosphere. *J.*  
801 *Geophys. Res.*, **111**, D22105, doi:10.1029/2006JD007304
- 802 Bell, M. A. and P. J. Lamb, 2006. Integration of weather system variability to multidecadal  
803 regional climate change: the West African Sudan-Sahel zone, 1951-98. *J. Climate*, **19**,  
804 5343-5365
- 805 Bharmal, N. A., A. Slingo, G. J. Robinson and J. J. Settle, 2008. Simulation of surface and top of  
806 atmosphere thermal fluxes and radiances from the RADAGAST experiment. *J. Geophys.*  
807 *Res.*, to be submitted for publication
- 808 Charney, J. G., 1975. Dynamics of deserts and drought in the Sahel. *Q. J. R. Meteorol. Soc.*, **101**,  
809 193-202
- 810 Comer, R. E., A. Slingo and R. P. Allan, 2007. Observations of the diurnal cycle of outgoing  
811 longwave radiation from the Geostationary Earth Radiation Budget instrument. *Geophys.*  
812 *Res. Lett.*, **34**, L02823, doi:10.1029/2006GL028229
- 813 Derrien, M., and H. Le Gléau, 2005. MSG/SEVIRI cloud mask and type from SAFNWC. *Int. J.*  
814 *Remote Sens.*, **26**, 4707-4732, DOI: 10.1080/01431160500166128
- 815 Dewitte, S., L. Gonzalez, N. Clerbaux, A. Ipe, C. Bertrand and B. De Paepe, 2008. The  
816 Geostationary Earth Radiation Budget Edition 1 data processing algorithms. *Advances in*  
817 *Space Research*, **41**, No. 11, 1906-1913
- 818 Harries, J. E. and 42 authors, 2005. The Geostationary Earth Radiation Budget (GERB) project.  
819 *Bull. Am. Meteorol. Soc.*, **86**, 945-960
- 820 Haywood, J. M, et al., 2008. Overview of the Dust and Biomass burning Experiment and African  
821 Monsoon Multidisciplinary Analysis Special Observing Period-0. *J. Geophys. Res.*,  
822 submitted for publication in DABEX special section
- 823 Holben, B. N., et al., 2001. An emerging ground-based aerosol climatology: Aerosol Optical  
824 Depth from AERONET, *J. Geophys. Res.*, **106**, 12067-12097
- 825 Kiehl, J. T. and Trenberth, K. E., 1997. Earth's annual global mean energy budget. *Bull. Amer.*  
826 *Meteorol. Soc.*, **78**, 197-208
- 827 Kollias, P., M. Miller and K. L. Johnson, 2008. Cloud and precipitation observations during the

828           2006 ARM Mobile Facility deployment in Niamey, Niger, Africa. *J. Geophys. Res.*, to be  
829           submitted for publication

830 Loeb, N. G., B. A. Wielicki, W. Su, K. Loukachine, W. Sun, T. Wong, K. J. Priestley, G.  
831           Matthews, W. F. Miller and R. Davies, 2007. Multi-instrument comparison of top-of-  
832           atmosphere reflected solar radiation. *J. Clim.*, **20**, 575-591

833 McFarlane, S. A., J. H. Mather and T. P. Ackerman, 2007. Analysis of tropical radiative heating  
834           profiles: A comparison of models and observations. *J. Geophys. Res.*, **112**, D14218,  
835           doi:10.1029/2006JD008290

836 McFarlane, S. A., E. I. Kassianov, J. Barnard, C. Flynn and T. P. Ackerman, 2008. Surface  
837           shortwave aerosol radiative forcing during the ARM Mobile Facility deployment in  
838           Niamey, Niger. *J. Geophys. Res.*, to be submitted for publication

839 Michalsky, J., E. Dutton, M. Rubes, D. Nelson, T. Stoffel, M. Wesley, M. Splitt and J. DeLuisi,  
840           1999. Optimal measurement of surface shortwave irradiance using current instrumentation.  
841           *J. Atmos. Ocean. Technol.*, **16**, 55-69

842 Miller, M. A. and A. Slingo, 2007. The ARM Mobile Facility and its first international  
843           deployment: measuring radiative flux divergence in West Africa. *Bull. Am. Meteorol. Soc.*,  
844           **88**, 1229-1244

845 Miller, R. L., J. Barnard, E. Kassianov and A. Slingo, 2008. Seasonal contrasts in the surface  
846           energy balance of the Sahel. *J. Geophys. Res.*, to be submitted for publication

847 Ohmura, A., et al., 1998. Baseline Surface Radiation Network (BSRN/WCRP): New precision  
848           radiometry for climate research. *Bull. Am. Meteorol. Soc.*, **79**, 2115-2136

849 Prata, A. J., 1996. A new long-wave formula for estimating downward clear-sky radiation at the  
850           surface. *Q. J. R. Meteorol. Soc.*, **122**, 1127-1151

851 Prospero, J. M., P. Ginoux, O. Torres, S. E. Nicholson and T. E. Gill, 2002. Environmental  
852           characterization of global sources of atmospheric soil dust identified with the Nimbus 7  
853           total ozone mapping spectrometer (TOMS) absorbing aerosol product. *Rev. Geophys.*, **40**,  
854           1002, doi:10.1029/2000RG000095

855 Ramana, M. V., V. Ramanathan, D. Kim, G. C. Roberts and C. E. Corrigan, 2007. Albedo,  
856           atmospheric solar absorption and heating rate measurements with stacked UAVs. *Q. J. R.*  
857           *Meteorol. Soc.*, **133**, 1913-1931

858 Ramaswamy, V. and S. M. Freidenreich, 1992. A study of broadband parameterizations of the  
859 solar radiative interactions with water vapor and water drops. *J. Geophys. Res.*, **97**, D11,  
860 11487-11512

861 Randall, D. A., et al., 2007. Climate Models and Their Evaluation. In: *Climate Change 2007: The*  
862 *Physical Science Basis. Contribution of Working Group I to the Fourth Assessment Report*  
863 *of the Intergovernmental Panel on Climate Change* [Solomon, S., D. Qin, M. Manning, Z.  
864 Chen, M. Marquis, K. B. Averyt, M. Tignor and H. L. Miller (eds.)]. Cambridge University  
865 Press, Cambridge, United Kingdom and New York, NY, USA

866 Redelsperger, J.-L., C. D. Thorncroft, A. Diedhiou, T. Lebel, D. J. Parker and J. Polcher, 2006.  
867 African Monsoon Multidisciplinary Analysis. An international research project and field  
868 campaign. *Bull. Am. Meteorol. Soc.*, **87**, 1739-1746

869 Schmetz, J., P. Pili, S. Tjemkes, D. Just, J. Kerkman, S. Rota, and A. Ratier, 2002. An  
870 introduction to Meteosat Second Generation (MSG). *Bull. Am. Meteorol. Soc.*, **83**, 977-992

871 Settle, J. J., N. A. Bharmal, G. J. Robinson and A. Slingo, 2008. Bounding the uncertainty of flux  
872 divergence calculations in RADAGAST. *J. Geophys. Res.*, to be submitted for publication

873 Slingo, A., et al., 2006. Observations of the impact of a major Saharan dust storm on the  
874 atmospheric radiation balance. *Geophys. Res. Lett.*, **33** (24), L24817, doi:  
875 10.1029/2006GL027869

876 Slingo, A., et al., 2008. Overview of observations from the RADAGAST experiment in Niamey,  
877 Niger. Part 1: Meteorology and thermodynamic variables. *J. Geophys. Res.*, submitted for  
878 publication

879 Stackhouse, P. W., S. K. Gupta, S. J. Cox, J. C. Mikowitz, T. Zhang and M. Chiacchio, 2004. 12-  
880 year surface radiation budget data set. *GEWEX News*, **14**, 10-12

881 Stephens, G. L., 1990. On the relationship between water vapor over the oceans and sea surface  
882 temperature. *J. Clim.*, **3**, 634-645

883 Stephens, G. L., A. Slingo, M. J. Webb, P. J. Minnett, P. H. Daum, L. Kleinman, I. Wittmeyer  
884 and D. A. Randall, 1994. Observations of the Earth's radiation budget in relation to  
885 atmospheric hydrology. 4. Atmospheric column radiative cooling over the world's oceans.  
886 *J. Geophys. Res.*, **99**, 18585-18604

887 Turner, D. D., 2008. Ground-based infrared retrievals of optical depth, effective radius, and  
888 composition of airborne mineral dust above the Sahel. *J. Geophys. Res.*, submitted for  
889 publication

890 Wong, T., B. A. Wielicki, R. B. Lee, G. L. Smith, K. A. Bush, and J. K. Willis, 2006.  
891 Reexamination of the observed decadal variability of the earth radiation budget using  
892 altitude-corrected ERBE/ERBS nonscanner WFOV data. *J. Clim.* **19**, 4028-4040

893 Zhang, Y., W. B. Rossow, A. A. Lacis, V. Oinas and M. I. Mishchenko, 2004. Calculation of  
894 radiative fluxes from the surface to top of atmosphere based in ISCCP and other global data  
895 sets: Refinements of the radiative transfer model and the input data. *J. Geophys. Res.*, 109,  
896 D19105, doi:10.1029/2003JD004457

897

898 **Figure captions**

899 Figure 1. a) timeseries of cloud fraction from the CLMK cloud mask derived from SEVIRI data  
900 for the GERB ARG pixel over Niamey (solid) and from the *Kollias et al.* [2008] cloud data  
901 (dashed). Note that the latter data are only available from mid-March. b) timeseries of aerosol  
902 optical thickness at 870nm from the AERONET site at Banizoumbou. The day number in 2006 is  
903 shown along the bottom of each plot. The dashed vertical lines denote the boundaries between the  
904 calendar months, the first letters of which are shown along the top of each plot.

905 Figure 2. Timeseries of the surface a) downwelling, b) upwelling and c) net longwave fluxes,  
906 measured at the AMF Niamey airport site. The day number in 2006 is shown along the bottom of  
907 each plot. The dashed vertical lines denote the boundaries between the calendar months, the first  
908 letters of which are shown along the top of each plot.

909 Figure 3. Timeseries of the surface a) downwelling, b) upwelling and c) net shortwave fluxes,  
910 measured at the AMF Niamey airport site. The day number in 2006 is shown along the bottom of  
911 each plot. The dashed vertical lines denote the boundaries between the calendar months, the first  
912 letters of which are shown along the top of each plot.

913 Figure 4. Timeseries of the top of atmosphere a) outgoing longwave radiation (OLR) measured  
914 by GERB, b) reflected shortwave radiation measured by GERB and c) calculated incoming  
915 shortwave radiation. The day number in 2006 is shown along the bottom of each plot. The dashed  
916 vertical lines denote the boundaries between the calendar months, the first letters of which are  
917 shown along the top of each plot.

918 Figure 5. a) scatter plot of the downwelling longwave flux at the surface, measured at the AMF  
919 Niamey airport site, against surface air temperature. The data points are color coded according to  
920 whether they were measured during the dry or wet seasons. Open squares denote days with cloud,  
921 according to the SEVIRI cloud mask. The dotted lines show the fluxes given by the Prata formula  
922 (Equations 1 and 2) for several values of the column water vapor (cm). b) simplified  
923 representation of the trajectory of the measurements through the year (see text).

924 Figure 6. a) scatter plot of the downwelling longwave flux at the surface, measured at the AMF  
925 Niamey airport site, against column water vapor. The data points are color coded according to  
926 whether they were measured during the dry or wet seasons. Open squares denote days with cloud,  
927 according to the SEVIRI cloud mask. The dotted lines show the fluxes given by the Prata formula

928 (Equations 1 and 2) for several values of the surface air temperature (K). b) simplified  
929 representation of the trajectory of the measurements through the year (see text).

930 Figure 7. Scatter plots of the net longwave flux at the surface, measured at the AMF Niamey  
931 airport site, against a) surface air temperature and b) column water vapor. In each panel, the data  
932 points are color coded according to whether they were measured during the dry or wet seasons.  
933 Open squares denote days with cloud, according to the SEVIRI cloud mask.

934 Figure 8. Scatter plots of the outgoing longwave radiation (OLR), measured by GERB, against a)  
935 surface air temperature and b) column water vapor. In each panel, the data points are color coded  
936 according to whether they were measured during the dry or wet seasons. Open squares denote  
937 days with cloud, according to the SEVIRI cloud mask.

938 Figure 9. Scatter plots of a) the downwelling longwave flux at the surface, measured at the AMF  
939 Niamey airport site and of b) the outgoing longwave radiation (OLR), measured by GERB,  
940 against the aerosol extinction at 870nm (defined by Equation 3). In each panel, the data points are  
941 color coded according to whether they were measured during the dry or wet seasons. Points are  
942 only plotted for days without cloud, according to the SEVIRI cloud mask. The dotted lines show  
943 the fluxes simulated by *Turner* [2008] for Kaolinite spheres (see text for details).

944 Figure 10. Scatter plots of the ratio of the downwelling shortwave flux at the surface, measured at  
945 the AMF Niamey airport site, to the insolation at the TOA, against a) the CWV and b) the aerosol  
946 extinction at 870nm (defined by Equation 3). In each panel, the data points are color coded  
947 according to whether they were measured during the dry or wet seasons. In a), open squares  
948 denote days with cloud, according to the SEVIRI cloud mask, and the dotted line shows the  
949 dependence of the water vapor transmittance on CWV, given by a simple parametrization (see  
950 text for details). For clarity, this line has been offset in the vertical so that it lies just above the  
951 data points. In b), points are only plotted for days without cloud, according to the SEVIRI cloud  
952 mask, and the dashed lines show the transmittances given by Equations 4 and 5. For clarity, these  
953 lines have been offset in the vertical to lie above most of the data points.

954 Figure 11. Scatter plots of the ratio of the reflected shortwave flux at the TOA, measured by  
955 GERB, to the insolation at the TOA, against a) the CWV and b) the aerosol extinction at 870nm  
956 (defined by Equation 3). In each panel, the data points are color coded according to whether they  
957 were measured during the dry or wet seasons. In a), open squares denote days with cloud,

958 according to the SEVIRI cloud mask. In b), points are only plotted for days without cloud,  
959 according to the SEVIRI cloud mask.

960 Figure 12. Timeseries of the longwave radiative divergences, calculated from the component  
961 fluxes, for the Earth-atmosphere system as a whole (dotted), for the surface (dashed) and for the  
962 atmosphere (solid). The day number in 2006 is shown along the bottom of each plot. The dashed  
963 vertical lines denote the boundaries between the calendar months, the first letters of which are  
964 shown along the top of each plot.

965 Figure 13. Timeseries of the shortwave radiative divergences, calculated from the component  
966 fluxes, for the Earth-atmosphere system as a whole (dotted), for the surface (dashed) and for the  
967 atmosphere (solid). The day number in 2006 is shown along the bottom of each plot. The dashed  
968 vertical lines denote the boundaries between the calendar months, the first letters of which are  
969 shown along the top of each plot.

970 Figure 14. Scatter plots of the longwave radiative divergence across the atmosphere against a) air  
971 temperature and b) column water vapor. In each panel, the data points are color coded according  
972 to whether they were measured during the dry or wet seasons. Open squares denote days with  
973 cloud, according to the SEVIRI cloud mask.

974 Figure 15. Scatter plot of the longwave radiative divergence across the atmosphere against the  
975 aerosol extinction at 870nm (defined by Equation 3). The data points are color coded according  
976 to whether they were measured during the dry or wet seasons. Points are only plotted for days  
977 without cloud, according to the SEVIRI cloud mask.

978 Figure 16. Scatter plots of the shortwave radiative divergence across the atmosphere against a)  
979 column water vapor and b) aerosol extinction. In each panel, the data points are color coded  
980 according to whether they were measured during the dry or wet seasons. In a), open squares  
981 denote days with cloud, according to the SEVIRI cloud mask. In b), points are only plotted for  
982 days without cloud, according to the SEVIRI cloud mask.

983 Figure 17. Timeseries of the net radiative divergences, obtained by adding the longwave and  
984 shortwave components, for the Earth-atmosphere system as a whole (dotted), for the surface  
985 (dashed) and for the atmosphere (solid). The day number in 2006 is shown along the bottom of  
986 each plot. The dashed vertical lines denote the boundaries between the calendar months, the first  
987 letters of which are shown along the top of each plot.

988 Figure 18. Scatter plots of the dimensionless parameters  $G$ ,  $F$  and  $1-G-F$  (see text for definition)  
989 against the column water vapor CWV. In each panel, the data points are color coded according to  
990 whether they were measured during the dry or wet seasons. Open squares denote days with cloud,  
991 according to the SEVIRI cloud mask.

992 Figure 19. Timeseries of the dimensionless parameters  $G$ ,  $F$  and  $1-G-F$  (see text for definition).  
993 The day number in 2006 is shown along the bottom of each plot. The dashed vertical lines denote  
994 the boundaries between the calendar months, the first letters of which are shown along the top of  
995 each plot.

996 **Table 1.** Annual means, and maximum and minimum daily mean values, of the radiative fluxes  
 997 and divergences ( $Wm^{-2}$ ) and of the near-surface air temperature, column water vapor (CWV) and  
 998 aerosol optical thickness (AOT). The sampling is the same for all the radiative fluxes and is  
 999 determined by the days when the OLR data are available.

1000

	Minimum	Mean	Maximum
OLR	170.2	266.3	320.9
Surface LW Down	312.7	392.7	447.5
Surface LW Up	441.2	496.1	561.1
Surface LW Net	-155.1	-103.4	-37.1
Atmospheric LW Divergence	-216.5	-162.8	-99.7
TOA SW In	338.3	407.3	444.2
TOA SW Out	85.8	125.8	269.6
TOA SW Net	170.6	281.1	342.5
Surface SW Down	59.3	250.1	351.2
Surface SW Up	9.3	57.5	84.6
Surface SW Net	50.0	192.7	267.7
Atmospheric SW Divergence	45.0	91.0	201.9
TOA Net Divergence	-62.5	14.6	101.8
Surface Net Divergence	7.0	89.2	180.3
Atmospheric Net Divergence	-124.7	-75.0	9.1
Air Temperature ( $^{\circ}C$ )	20.8	29.8	36.5
Column Water Vapor (cm)	0.49	2.89	5.70
Aerosol Optical Thickness	0.03	0.47	3.49

1001

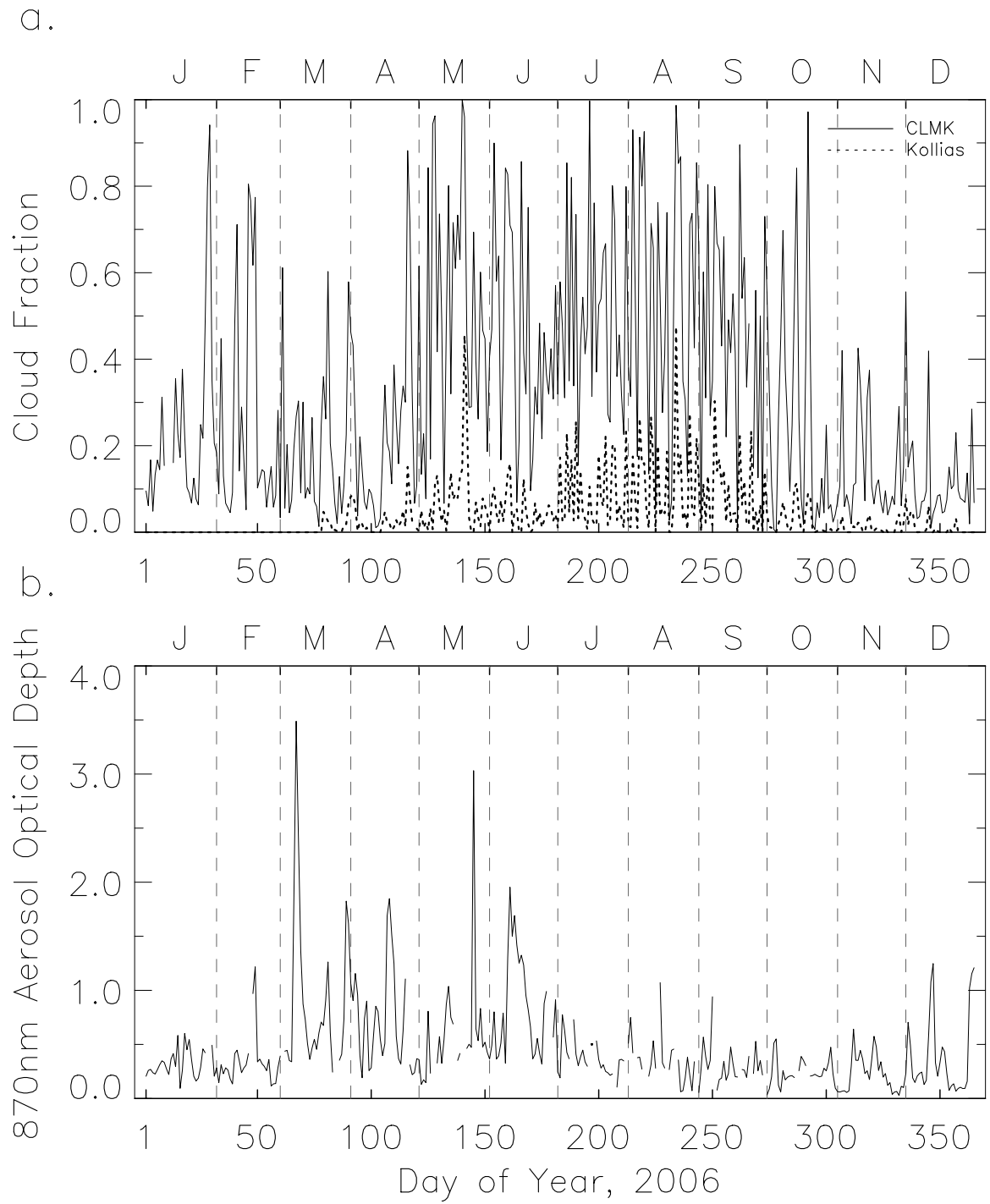


Figure 1

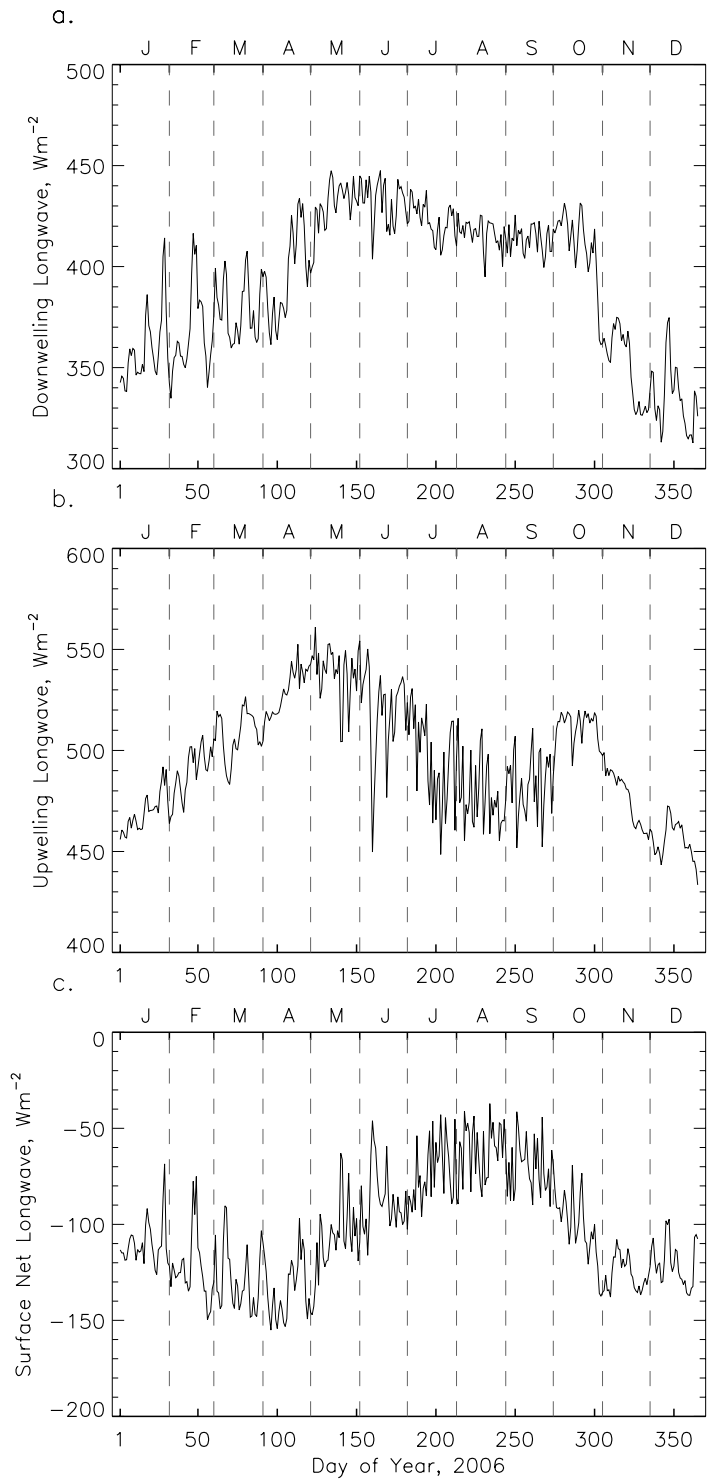


Figure 2

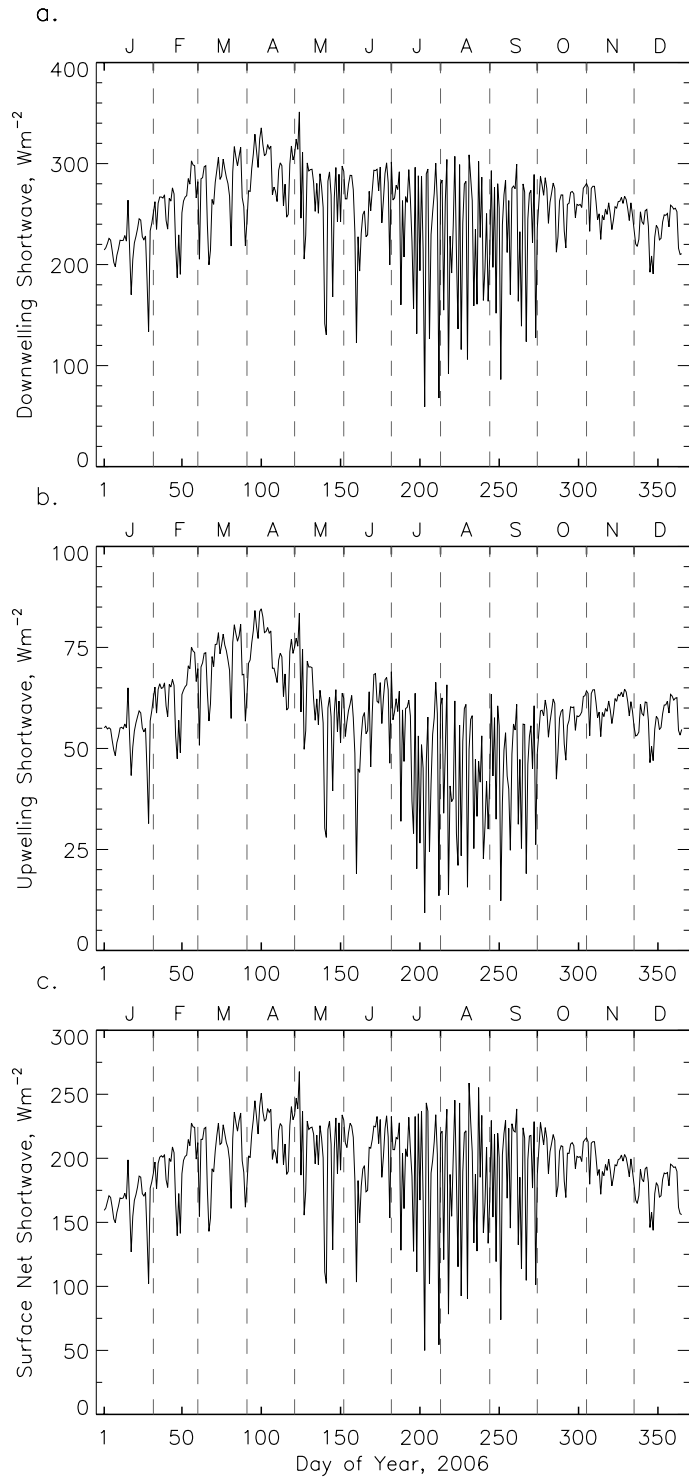


Figure 3

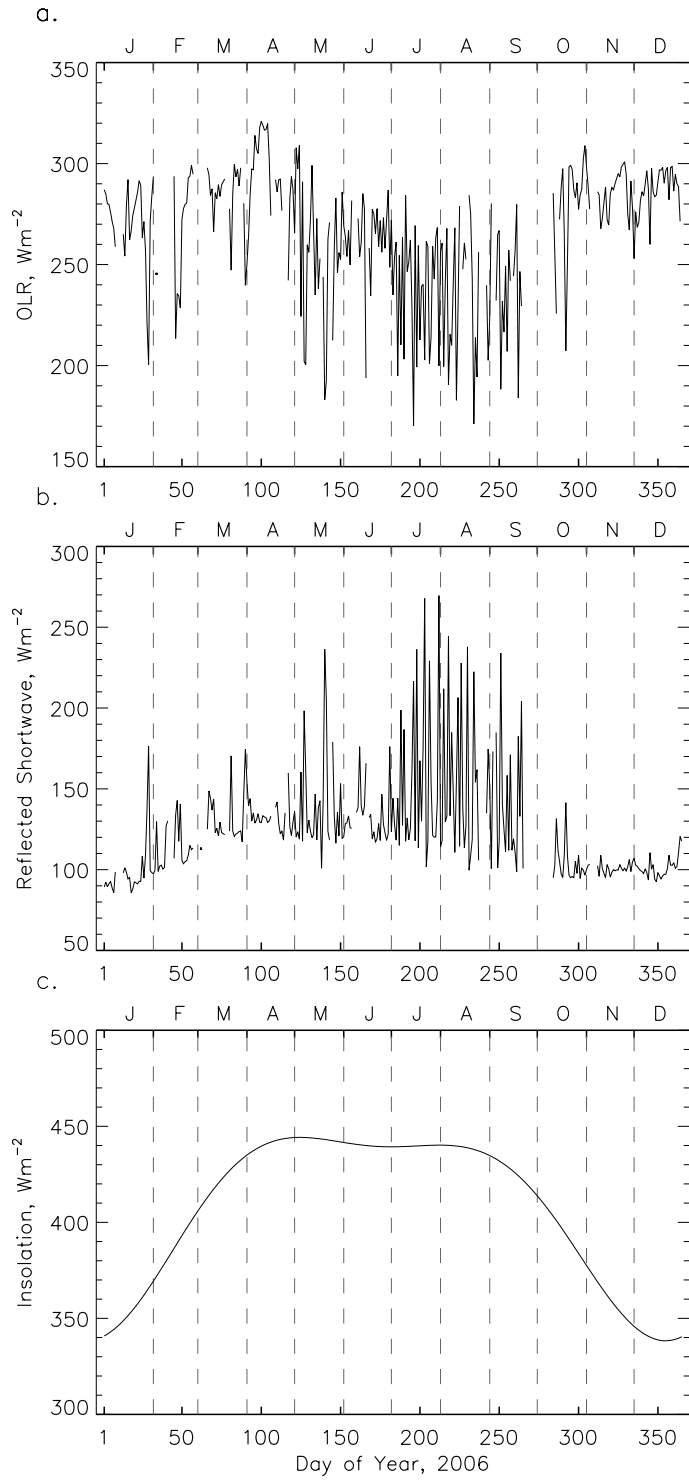


Figure 4

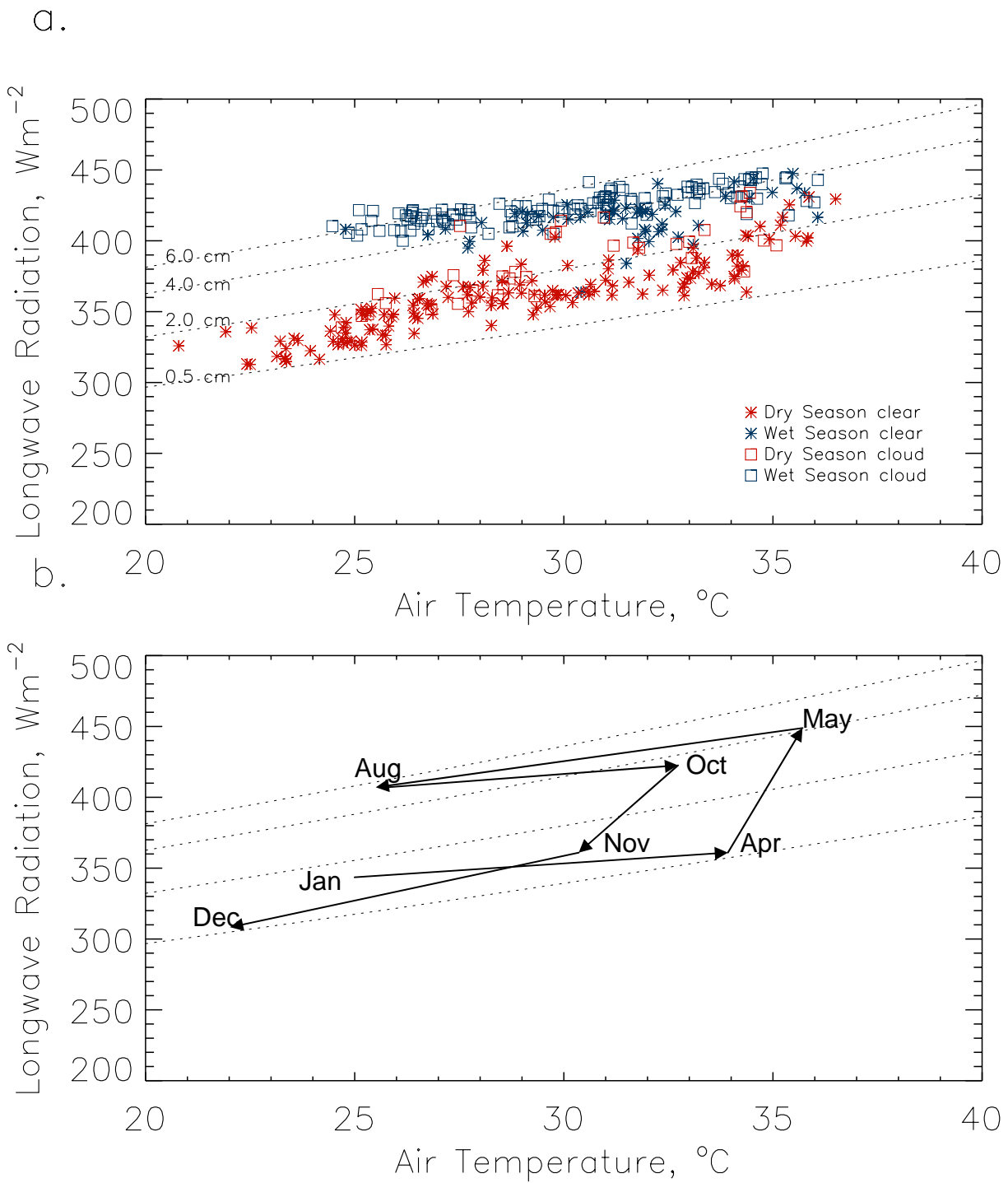


Figure 5

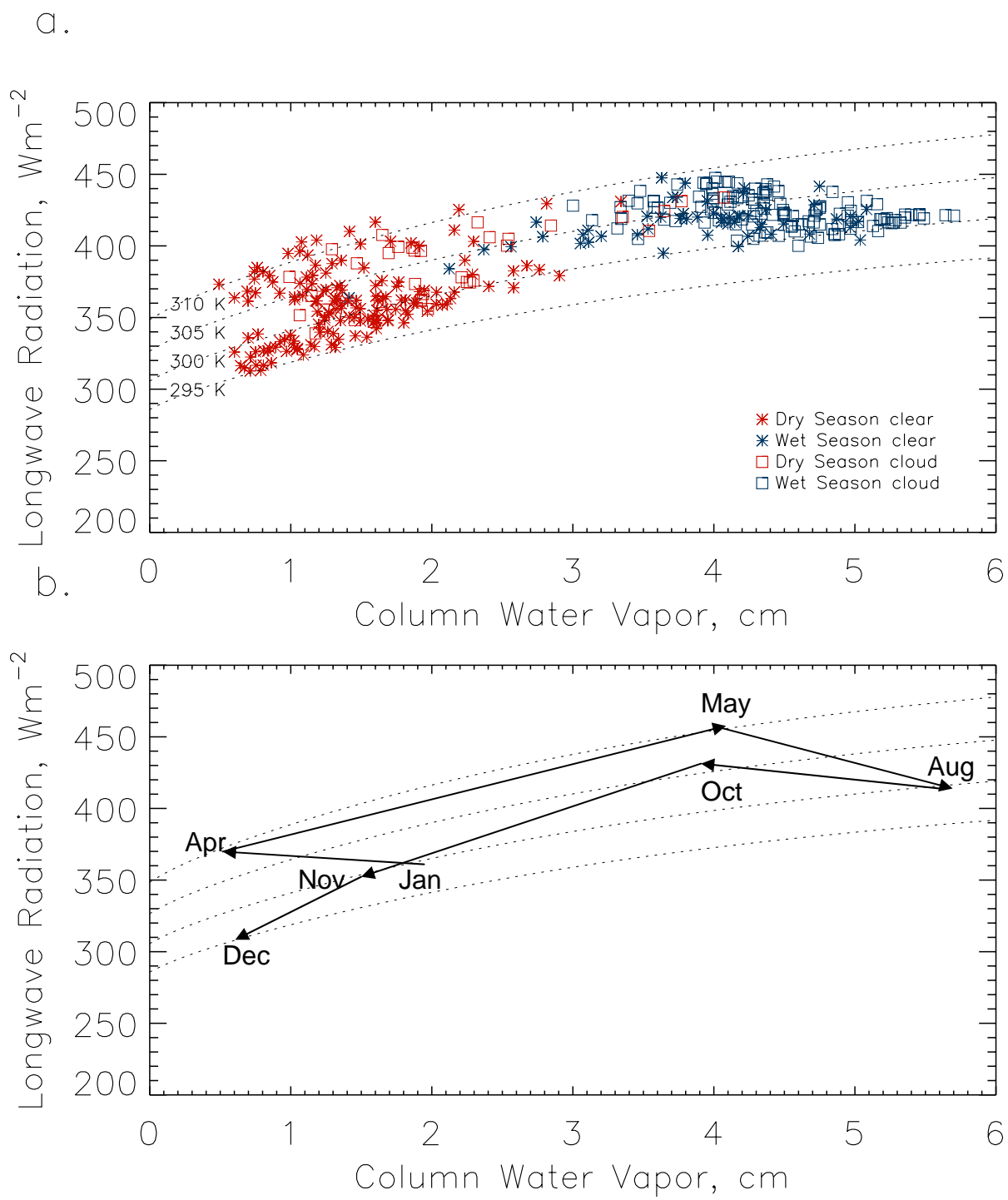


Figure 6

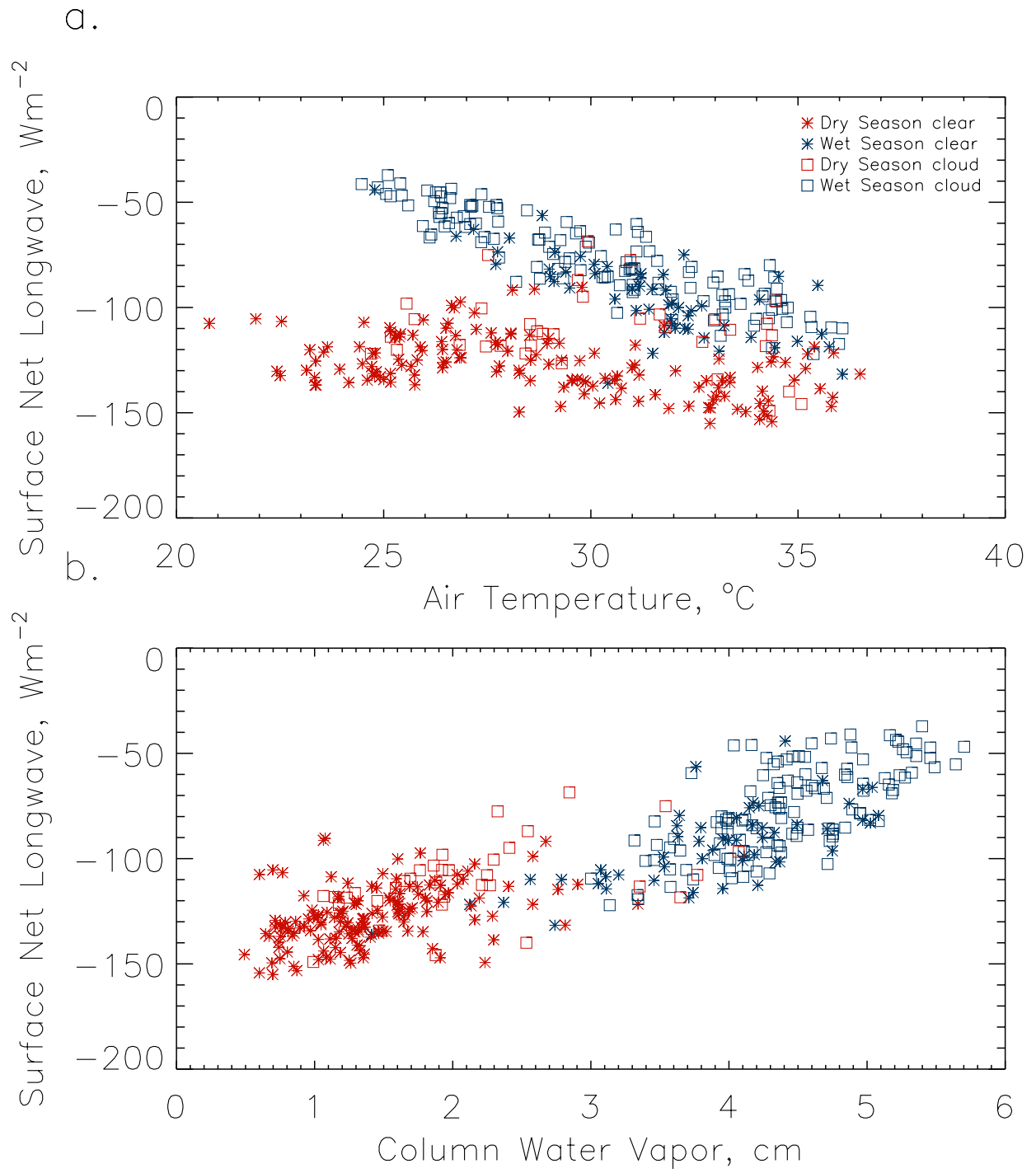


Figure 7

a.

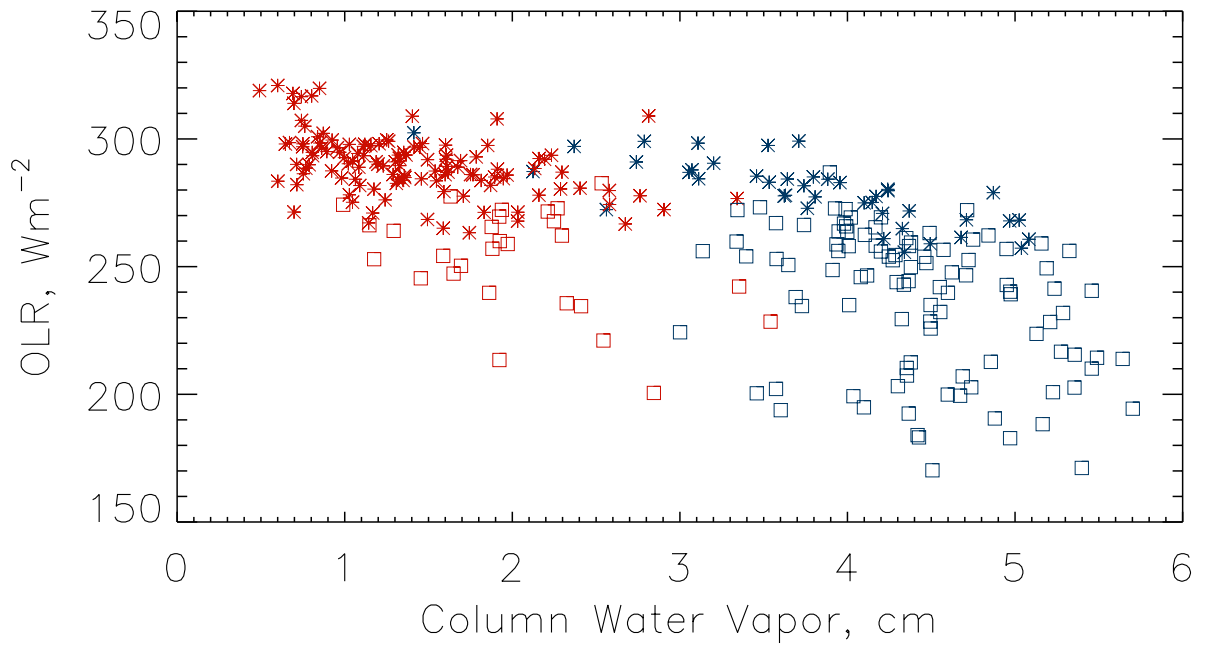
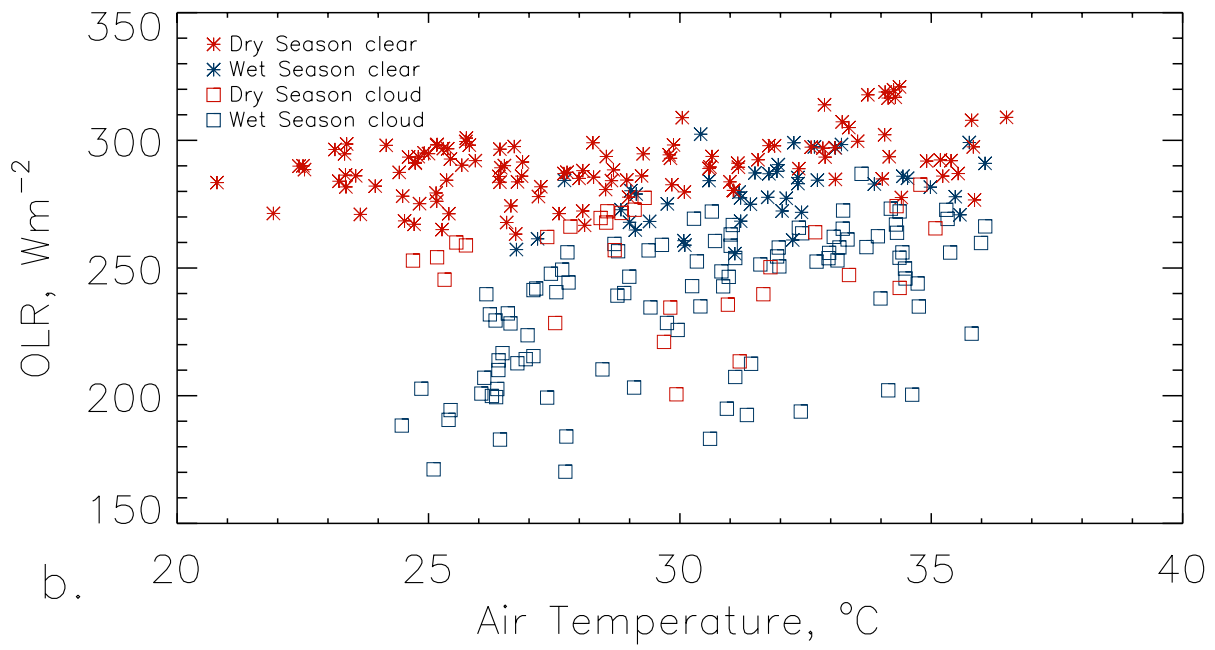


Figure 8

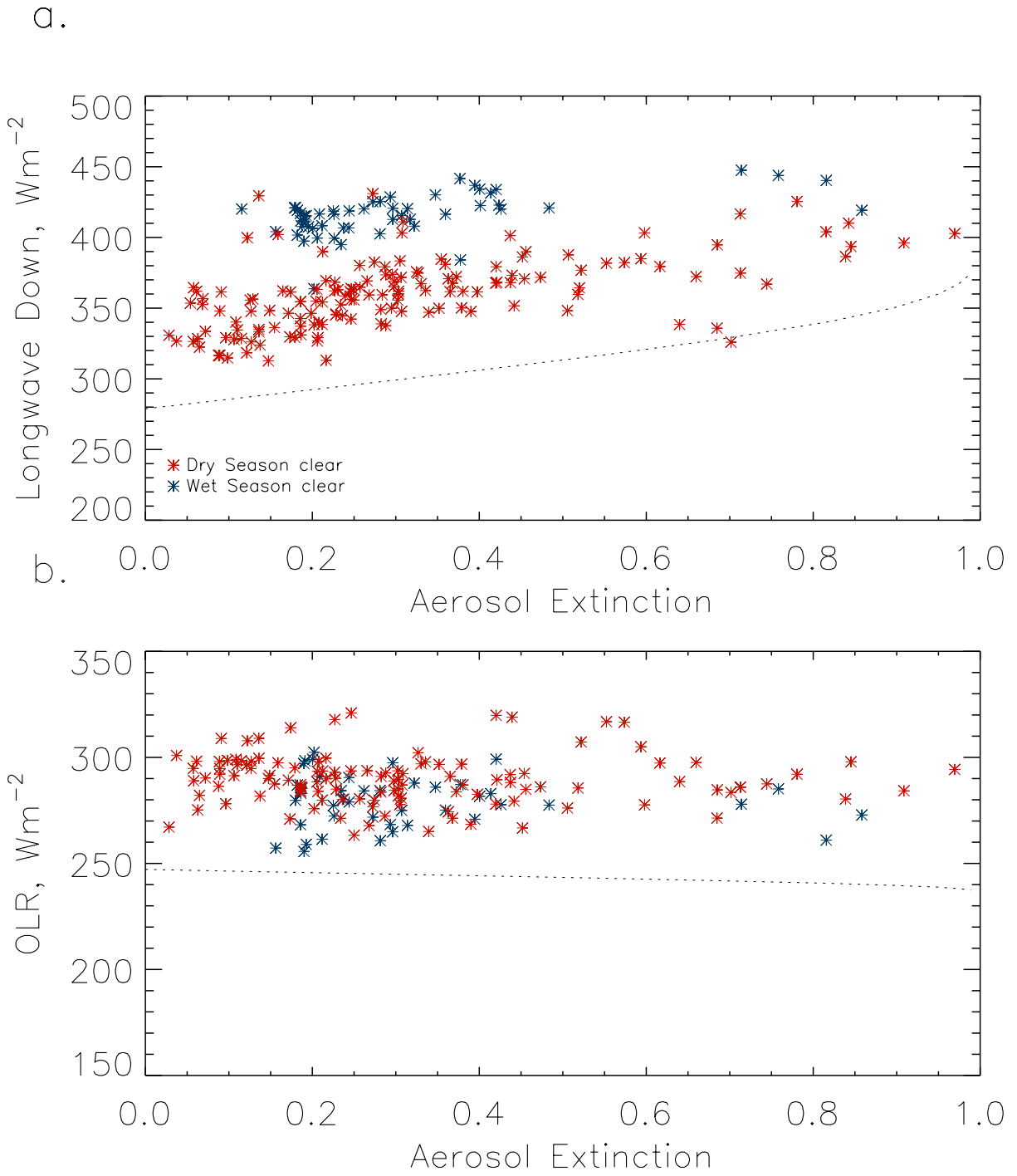
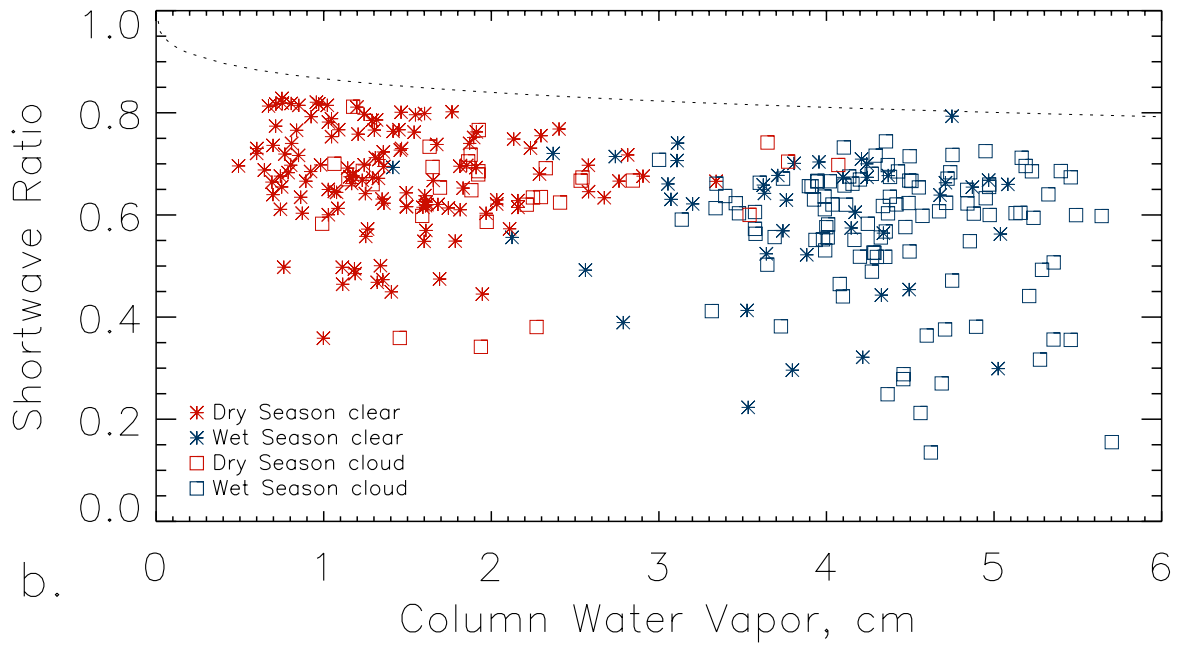


Figure 9

a.



b.

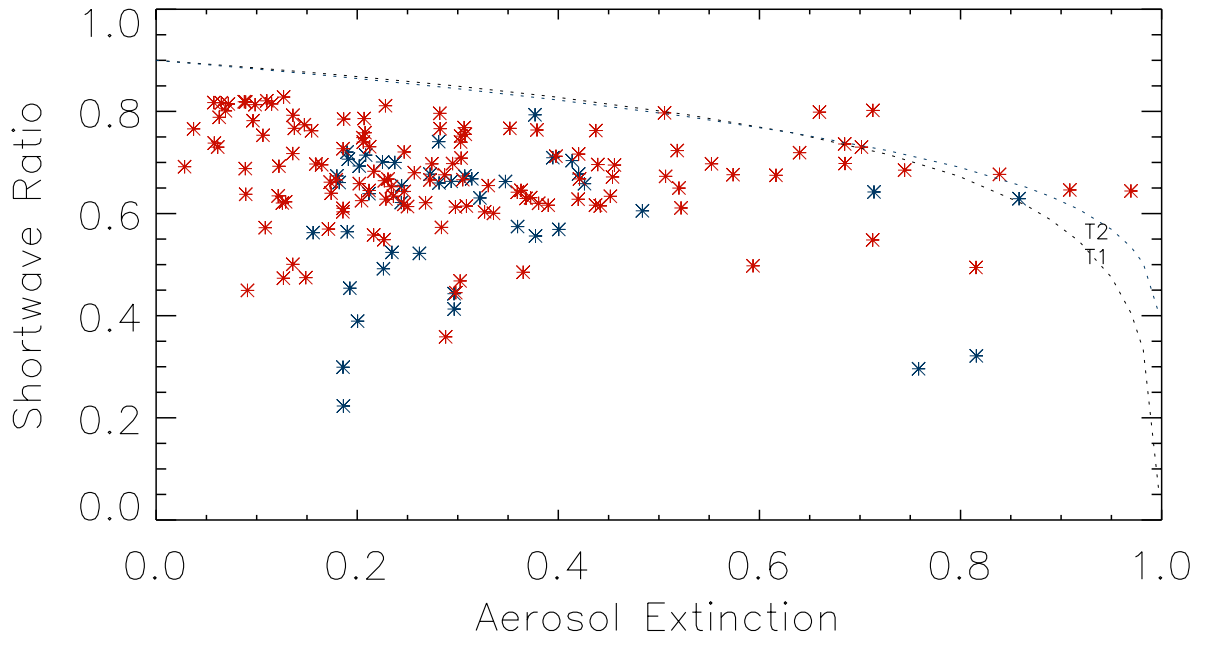
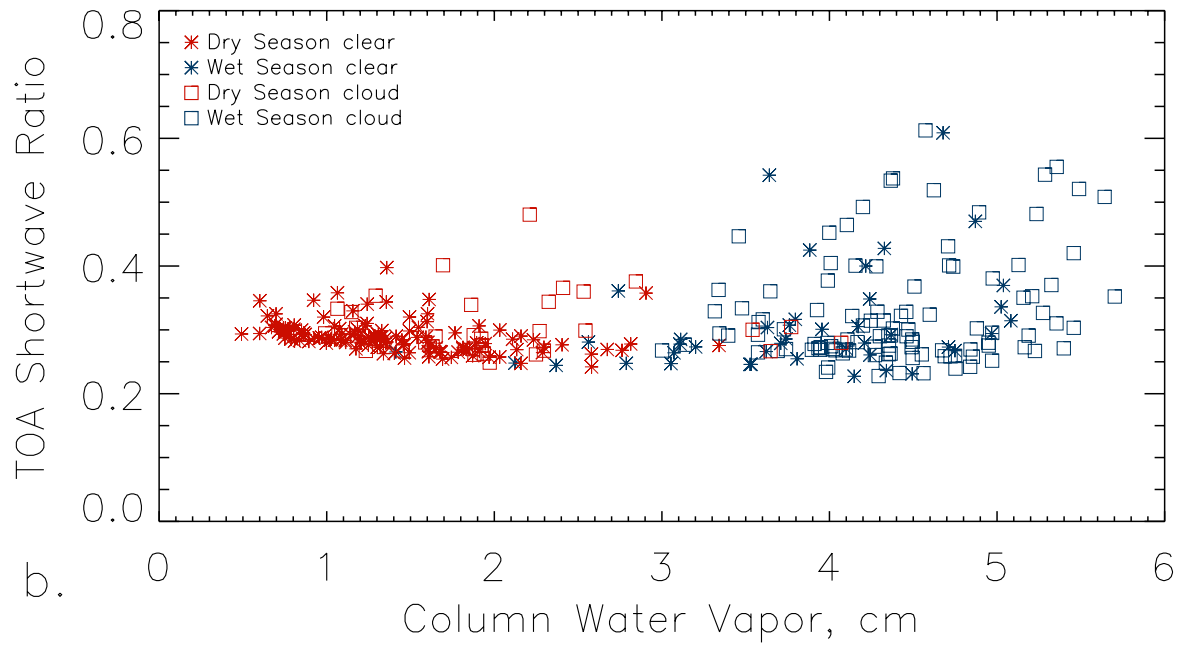


Figure 10

a.



b.

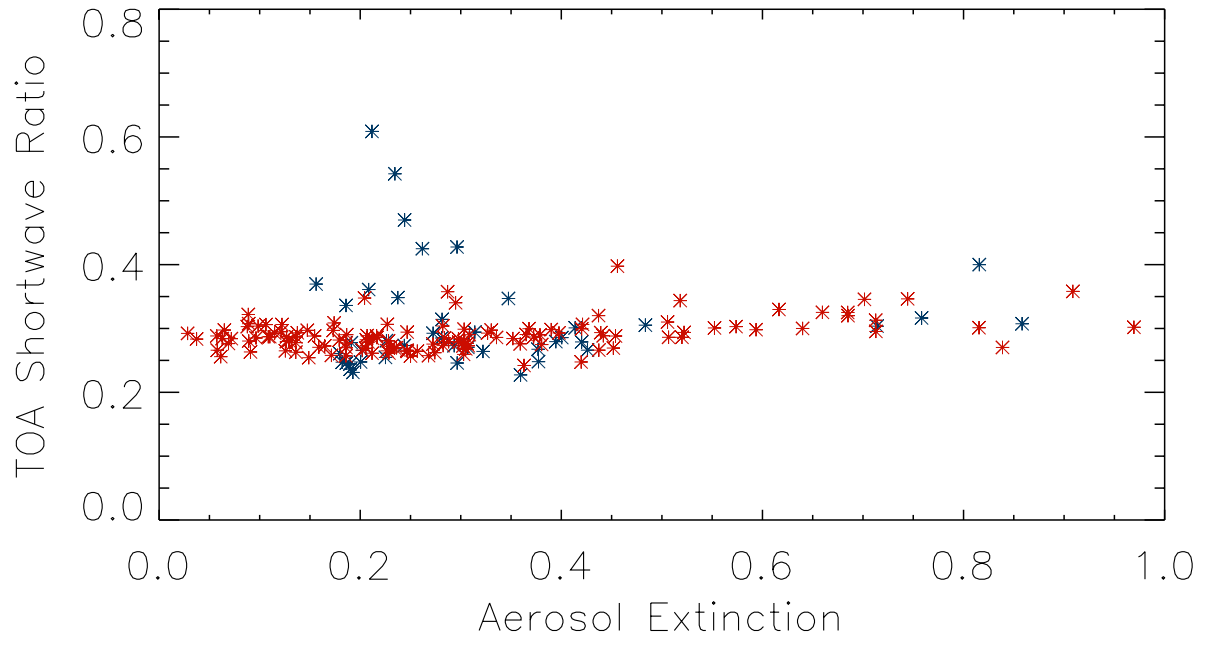


Figure 11

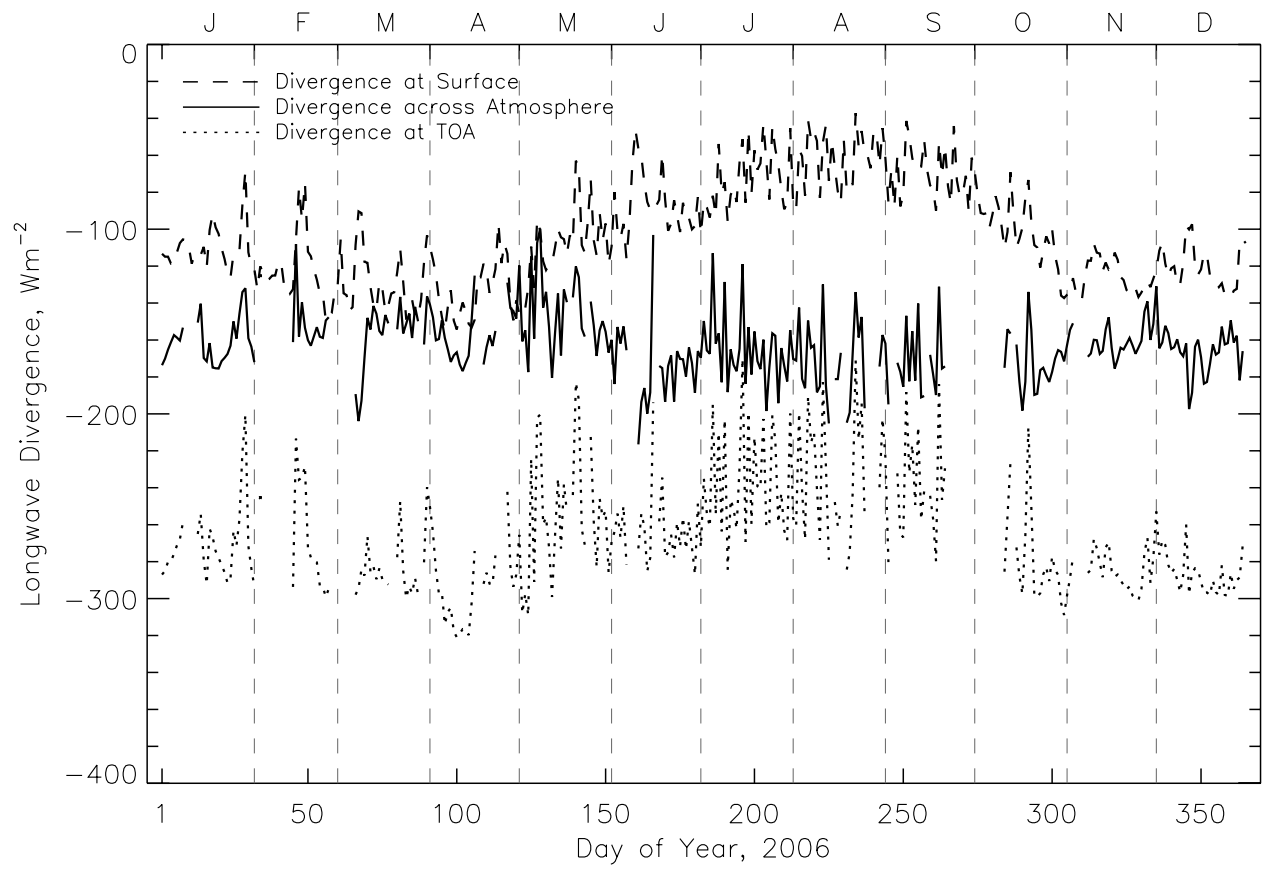


Figure 12

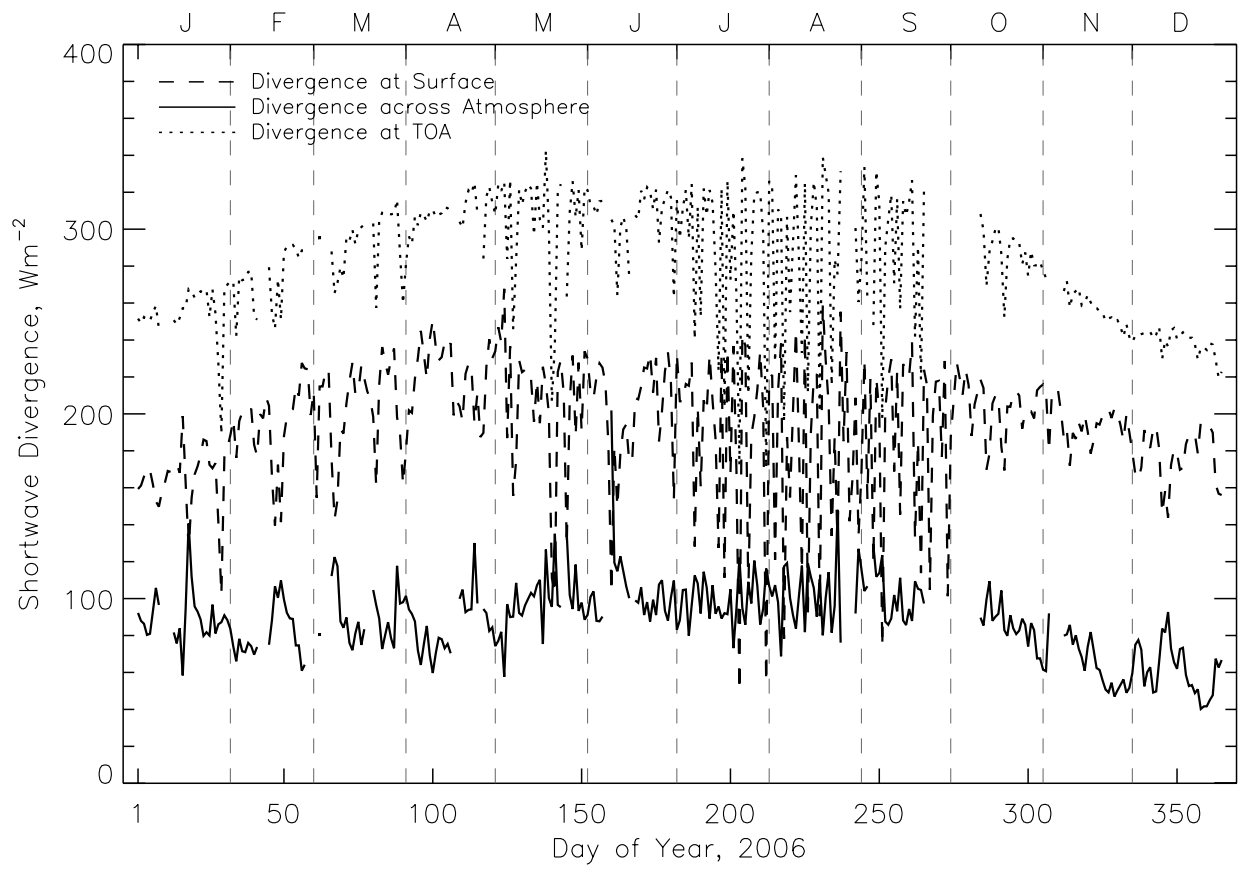


Figure 13

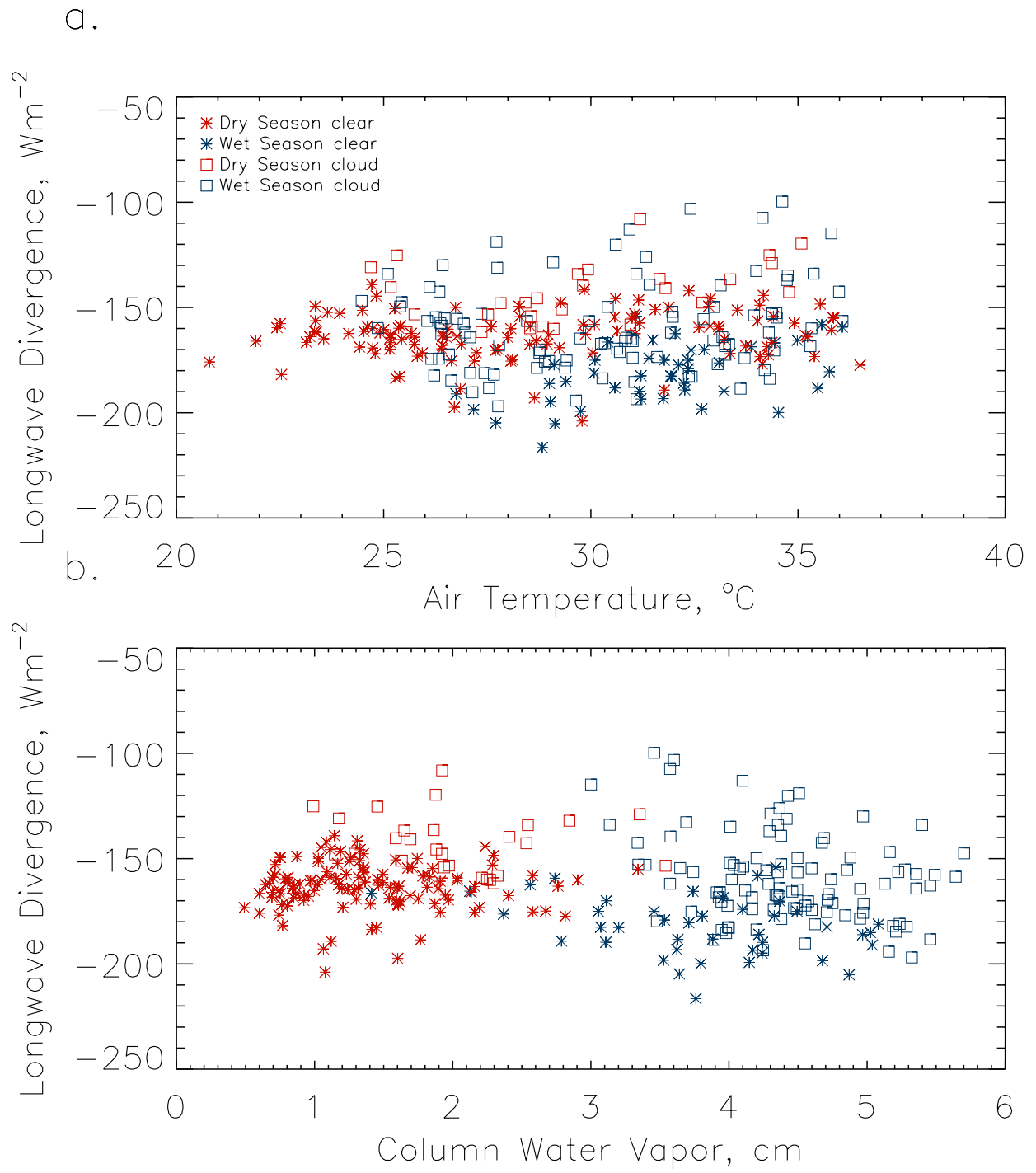


Figure 14

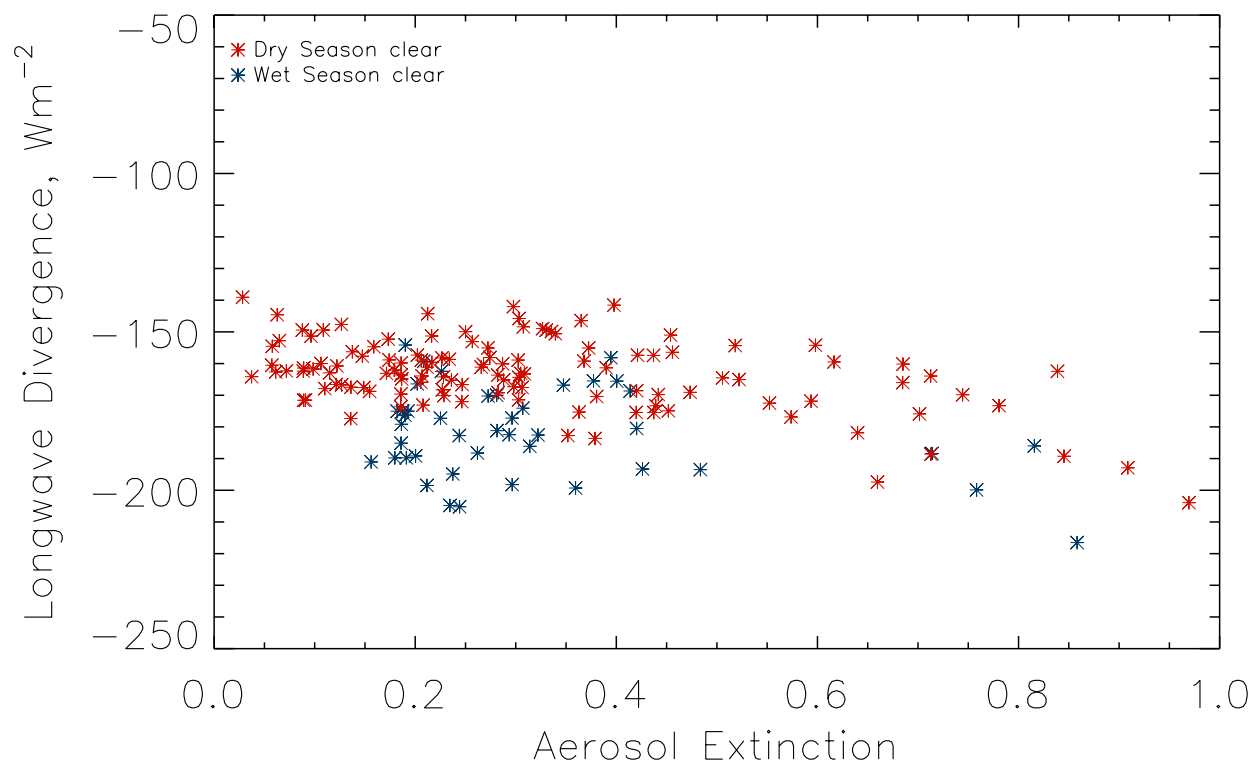


Figure 15

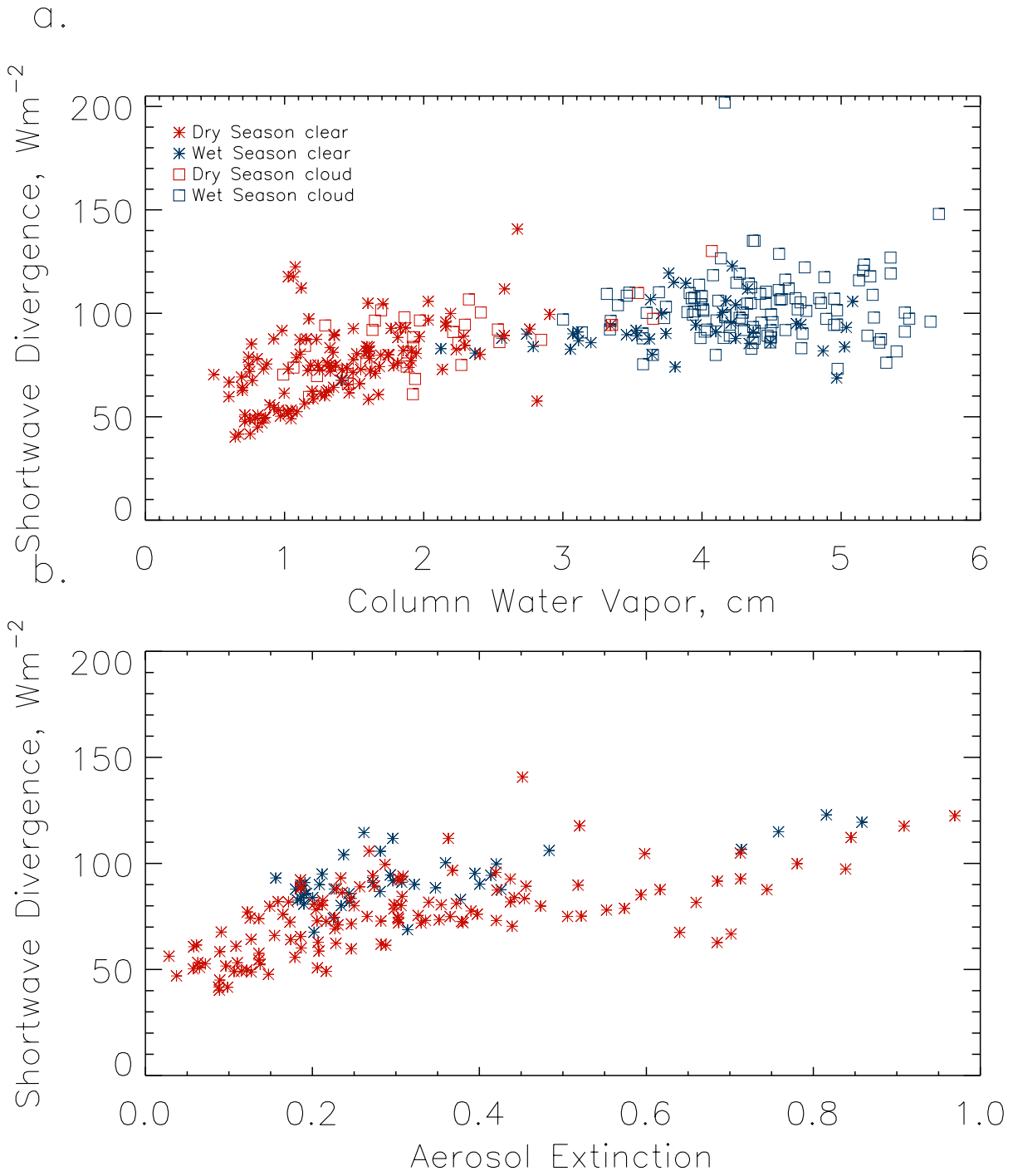


Figure 16

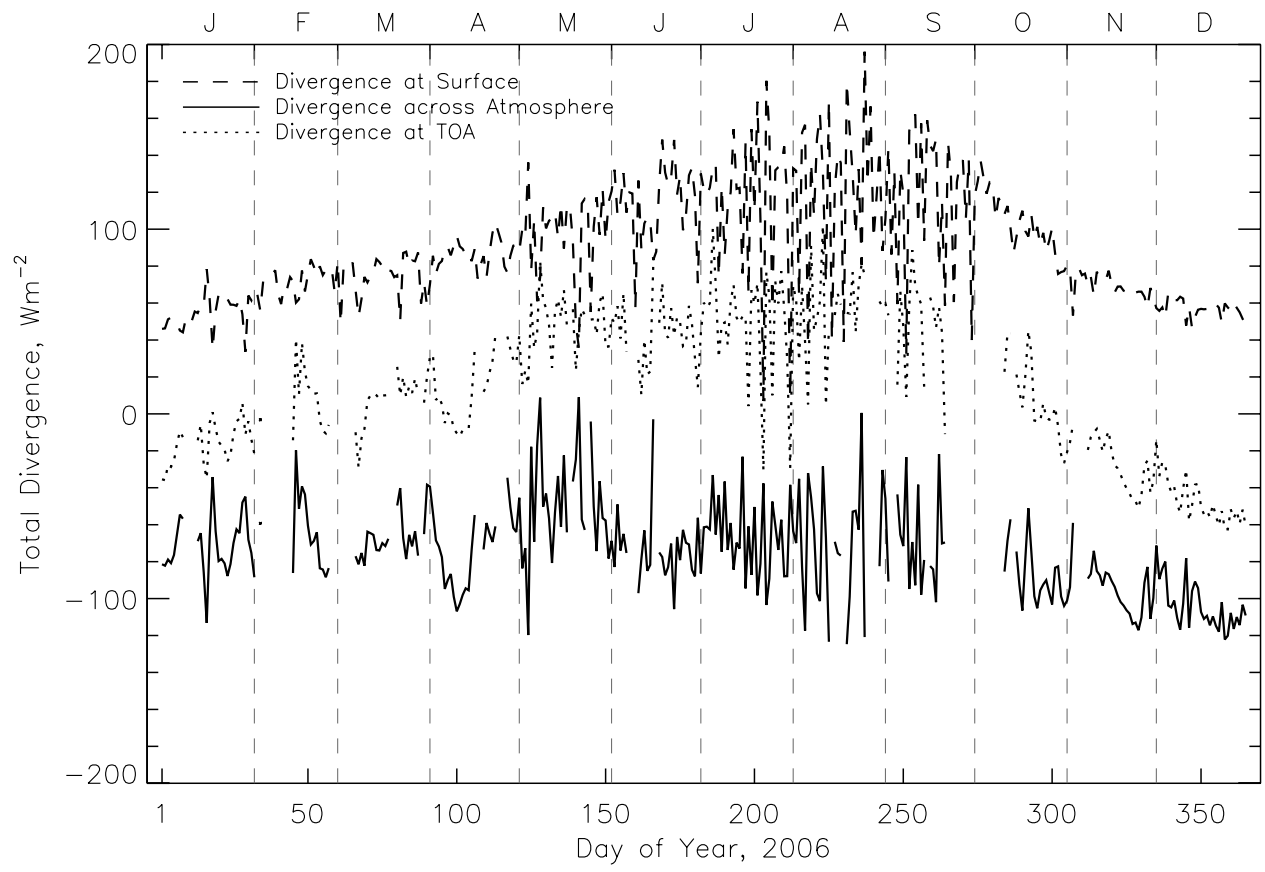


Figure 17



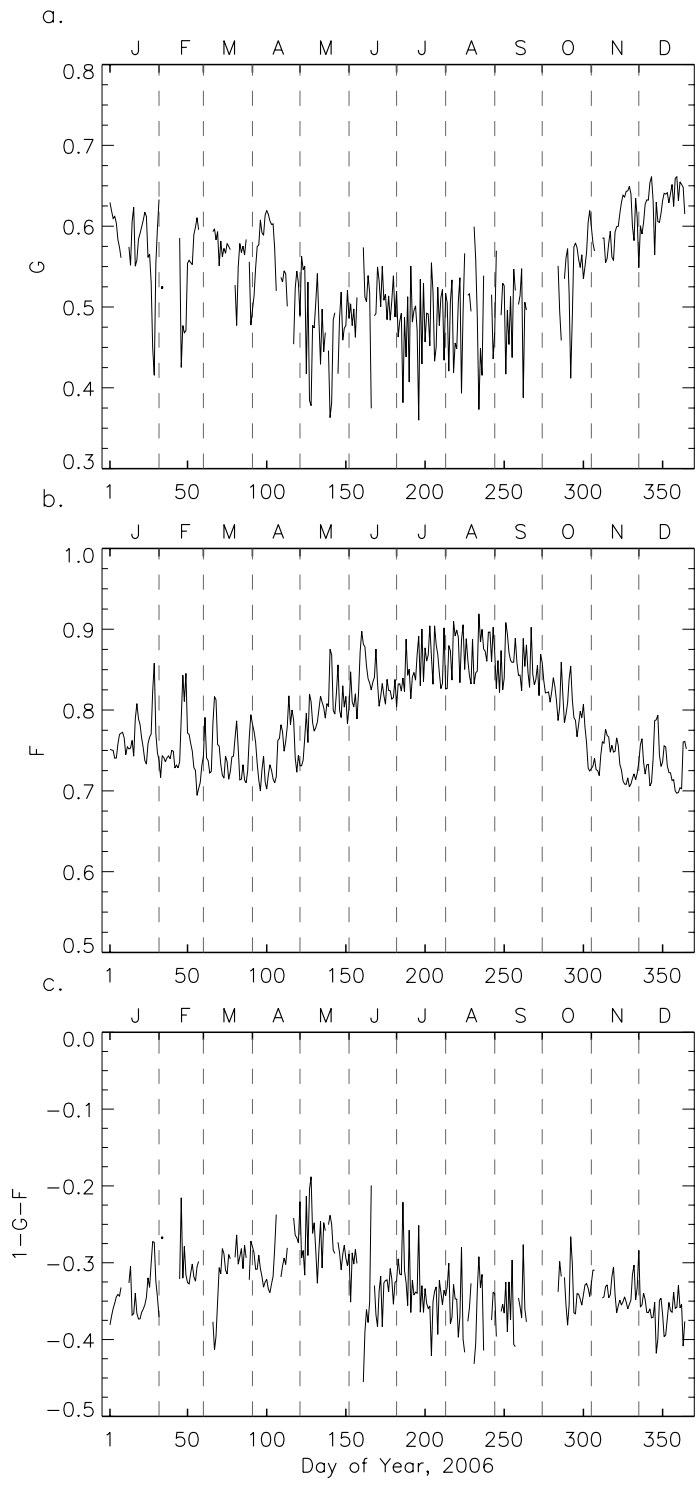


Figure 19